

A&A manuscript no.

(will be inserted by hand later)

Your thesaurus codes are:

08(02.12.1; 08.01.3; 08.05.1; 08.13.2)

ASTRONOMY
AND
ASTROPHYSICS
19.12.1996

Atmospheric NLTE-Models for the Spectroscopic Analysis of Luminous Blue Stars with Winds

A.E. Santolaya-Rey¹, J. Puls² and A. Herrero¹

¹ Instituto de Astrofísica de Canarias (IAC), La Laguna, Tenerife, Spain

² Universitäts-Sternwarte München, Scheinerstr. 1, D-81679 München, Germany

December 19, 1996

Abstract. We present a new, fast and easy to use NLTE line formation code for “unified atmospheres” with spherical extension and stellar winds, developed for the (routine) spectroscopic analysis of luminous blue stars, covering the spectral range from “A” to “O” and including central stars of planetary nebulae.

The major features of our code are: Data driven input of atomic models; consistent photospheric stratification including continuum radiative acceleration and photospheric extension; “ β -velocity law” for the wind; comoving frame or Sobolev plus continuum line transfer; fast solution algorithm for calculating line profiles, allowing for a consistent treatment of incoherent electron scattering.

We describe the code and perform thorough tests for models with H/He opacity, especially with respect to a comparison with plane-parallel, hydrostatic models in cases of thin winds. Our conclusions are:

Due in particular to our numerical treatment of the radiative transfer in the ionization and recombination integrals, the convergence rate of the solution algorithm is fast. The flux conservation is good, (maximum flux errors of order 2 to 3%), unless the atmospheric conditions are extreme, either with respect to mass-loss or to a large extension of the photosphere. (In these cases, our treatment of the temperature structure has to be improved). A comparison with plane-parallel results shows perfect agreement with the thin wind case. However, this comparison also reveals two interesting effects: First, the strength of the He I lines in hot O-stars is very sensitive to the treatment of electron scattering in the EUV. This might affect the effective temperature scale of early O spectral types. Second, the effects of photospheric extension become decisive for the gravity determination of stars close to the Eddington limit.

Finally, we demonstrate the differences in using the Sobolev vs. the comoving line transfer in the rate equations. We conclude that, in cases of moderate wind densities, comoving frame line transfer is inevitable for accurate quantitative work.

Key words: Line: formation – Stars: atmospheres – Stars: early-type – Stars: mass-loss

1. Introduction

Although it has in principle been possible for more than a decade and was promised in a variety of papers, the *quantitative* spectroscopy of large samples of “normal” hot stars accounting for radiatively accelerated outflows is still waiting to be undertaken, and has been performed only for a small number of mostly extreme and therefore untypical objects¹.

This problem and the corresponding lack of information related to the physical conditions in the upper HRD is a consequence of the different available atmospheric and line formation codes:

On the one hand, there is a class of code which has obtained such a high degree of sophistication that only a few people can use them. Furthermore, the computational time required to run a specific model becomes too large to cover a significant subspace of the total parameter space (which is at least of dimension three for a given He-content/metallicity) under consideration.

Alternative codes which are based on simpler physics (and hence have smaller turn-around times) suffer inevitably from some approximations which are insufficient in certain parameter ranges. In our opinion, the most severe restriction of these codes is the missing applicability to stars with thin or moderate winds, i.e., when the optical lines are still in absorption but already affected by the outflow. This failure typically arises because of an inappropriate formulation of the photospheric structure equations and/or the use of the Sobolev approximation for calculating radiative bound-bound rates.

¹ Here and in the following, we refrain from discussing WR-type stars, where the situation with respect to routine analysis methods is better (e.g., Schmutz et al. 1989; Hamann et al. 1991; Crowther et al. 1995a, 1995b) and from the analysis of LBVs, where the situation has considerably improved due to the work by de Koter et al. (1996).

In view of these difficulties, and in order to address the open questions related to stars with expanding atmospheres (see below), some years ago the authors of the present paper decided to develop a new NLTE line transfer code which should fulfill the following requirements:

- consistent atmospheric structure, especially in the sub-sonic/photospheric region.
- applicability over the entire upper HRD, beginning with stars of spectral type “A”
- reproduction of results from plane-parallel and hydrostatic models in cases of very thin winds
- “data driven” input of atomic models, following the philosophy of standard hydrostatic NLTE-codes (e.g., DETAIL, see below)
- easy to use, robust, fast and portable

The zero-version of this code was finished last year (Santolaya-Rey 1995), however, it did not completely match the above requirements. Meanwhile, we have worked on some additional improvements, mostly related to the photospheric structure and the incorporation of the comoving frame line transfer. Together with some of our collaborators, we have tested and applied the code for a variety of objects in the defined spectral range, from A-type Supergiants to O3-stars and central stars of planetary nebulae (CSPN). Since we are now convinced that it works robustly and reliably (at least with H/He opacity only), we want to describe its features in a first, more technical paper, before we present the results obtained with this code in some forthcoming papers.²

The underlying assumptions of a new program package always depend on the kind of questions one is seeking to address. Since we do not present any application to real stars in this paper, we will at least mention some of these questions which our working group is especially interested in to illustrate the chosen philosophy.

The mass and helium problem for O-stars. A careful analysis of a large sample of O-stars by Herrero et al. (1992) indicated that the spectroscopically derived masses of these stars are systematically lower than the masses predicted from standard stellar evolution. Moreover, the derived He abundance was found to be much larger than the model predictions. Both problems may vanish if one allows for an evolution with rotationally induced mixing (Langer & Maeder 1995). Nevertheless, a careful re-analysis for stars of low luminosity class remains to be done, since Herrero et al. performed their analysis on the basis of plane-parallel NLTE models, thus neglecting stellar wind effects. The inclusion of these effects might change the picture due to a different pressure stratification (the so-called “unified model atmosphere correction”, cf. Gabler et al. 1989; Puls et al. 1996) and additional wind emission, both of which increase the inferred masses to higher values. The latest investigations

by Lanz et al. (1996) confirm this expectation, and also the consistent FUV, UV and optical analysis of the extreme O3 If* star HD 93129A by Taresch et al. (1996) resulted in a mass in agreement with standard evolution. On the other hand, an analysis of HDE 226868, the optical counterpart of Cygnus X-1, using unified models (Herrero et al. 1995) indicated that the wind effects are not large enough to compensate for the whole mass discrepancy, and that they do not significantly affect the helium abundances. Thus, both open questions have to be clarified by extending the Herrero et al. sample to stars with significant mass-loss (which were deliberately left out) and the use of adequate analysis methods. In addition, the presence of the helium problem has to be corroborated by consistently analyzing the CNO abundances of these stars.

The “ β -problem”. As a by-product of the mass-loss determination performed by Puls et al. (1996), it turned out that O-stars with dense winds seem to have velocity fields which deviate from the predictions of standard radiation driven wind theory. If we characterize the typical velocity field in terms of the usual β -parameterization (e.g., Eq. 1), then we find from theory in all cases which are not very extreme a value of $\beta \approx 0.8$ (Pauldrach, Puls & Kudritzki 1986). However, the analysis of H α , which reacts very sensitively to the wind density and thus to the velocity law when in emission, revealed values of $\beta \gtrsim 1.0$ for the winds of supergiants. The same seems to be true for a number of CSPN (Méndez, priv.com.) This fact poses a significant problem both for the theory and for the analysis methods to be applied. For the former, the observed velocity structure remains to be explained (e.g., influence of multi-line effects?). For the latter, we have at least to account for the possibility that different β 's are present, since otherwise the spectroscopic results could lead to erroneous conclusions, as was demonstrated, e.g., by Schaerer & Schmutz (1994).

Calibration of the wind-momentum luminosity relation for AB supergiants. The so-called wind-momentum luminosity relation (WLR) of hot stars (see Kudritzki et al. 1995 and Puls et al. 1996 for a theoretical explanation) will most probably provide a new tool to determine an independent extragalactic distance scale by exploiting the dependence of radiatively driven winds on luminosity. While the calibration of this relation for O-type supergiants is almost finished (see Puls et al.), the continuation to spectral types B and A has suffered from the lack of a versatile and fast tool to perform the required NLTE diagnostics. By means of the code described here, however, our group has now made significant progress on AB supergiants and will present the results in a forthcoming paper.

Besides these central topics of immediate interest, a number of other, related points have to be clarified in the near future. We briefly mention the ongoing project of testing the theory of radiatively driven winds in the same spirit as outlined by Puls et al., however concentrating on the spectral ranges AB and on CSPN. This work, of course, will be done in parallel with the establishment of the corresponding WLRs.

² Actually, some of the results obtained by McCarthy et al. (1995) on the extreme A-Supergiant B-324 in M 33 are based on a preliminary version of the code described here.

The analysis of processes related to the effects of rotation and the presence of macro-structures (e.g., Massa et al. 1995, Prinja et al. 1995) in the winds of hot stars by means of detailed line diagnostics has made significant progress in the last years. Although we still assume that these effects are of only secondary influence on the gross behaviour and on the analysis of expanding atmospheres, there is no doubt that they are present and that they may contaminate the spectra and our conclusions. (See, e.g., Petrenz & Puls (1996) for the influence of rotation on the H_α mass-loss rates in the framework of the kinematic model provided by Bjorkman & Cassinelli (1993).) Because of the dominant NLTE conditions in the atmospheric regions under question, reliable predictions of the dependence of the occupation numbers on external parameters are urgently required. By means of (relatively) simple and fast calculations as discussed here, we can obtain much more insight concerning the dominating population processes of the participating levels and develop realistic line formation models.

With these problems to be solved in mind, the atmospheric model underlying our assumptions is as simple as possible, however accounts also for all (stationary) processes required to establish a consistent photospheric structure including spherical extension and continuum radiative acceleration. A thorough description (inclusive our atomic model) is given in Sect. 2 and Appendices A, B and C.

One of our most important objectives was to develop a *fast* code. Thus, the formulation of the bound-free rates (which mainly control the convergence behaviour) is decisive and presented in Appendix D. Also, we have reformulated the usually very time-consuming calculation of the formal integral in Sect. 2.4 and Appendix E.

In Sect. 3, we describe thorough tests of the code (convergence behaviour, flux conservation) and compare results from it to well-established plane-parallel results, both for the atmospheric structure (3.1) and strategic line profiles (3.4). The use of comoving frame transfer is most important for preciseness and the reproduction of profiles from plane-parallel models in cases of very thin winds. A comparison to alternative Sobolev transfer results is given in Sect. 3.5. Sect. 4 gives the conclusions, some caveats and future perspectives.

2. The stellar atmosphere code

2.1. Atomic data

In order to keep the treatment of atomic data in a rather flexible way, we are following the philosophy of the NLTE line formation code (hydrostatic, plane-parallel geometry) DETAIL (Butler & Giddings 1985): the atomic data file to be used as input contains all the information about the nature of the data included and how they must be treated. The line formation code is then *blind* to the atomic data, and these can be changed, if necessary, by a simple manipulation of the atomic data file and not of the program itself.

So far, we have used only hydrogen and helium, in the spirit of our principal objective of determining stellar and wind pa-

rameters. The inclusion of these two elements only does not, of course, allow the treatment of the metallic UV line blocking (e.g., Schaerer & Schmutz 1994; Pauldrach et al. 1994; Herrero 1994). However, by means of the completely *data-driven* nature of our program it is straightforward to include the missing opacities with almost no effort (as well as other elements important for diagnostic purposes, e.g., silicon for the determination of temperatures in B-stars). Obviously, this will constitute a natural progress of our work. For details of our atomic models and the applied broadening theory we refer the reader to Appendix A.

2.2. Atmospheric structure

Our atmospheric description refers to the well-established *standard model*, i.e., a stationary, smooth and spherically symmetric atmosphere neglecting any magnetic fields. For a detailed discussion of these approximations, see, e.g., Schaerer & Schmutz (1994) and Puls et al. (1996).

In order to set up the atmospheric stratification, we have developed a concept which allows us to treat the following constraints:

- The outer expanding atmosphere (wind) is specified by the stellar mass-loss rate \dot{M} , the terminal velocity v_∞ and a prescribed velocity parameter β , such that the velocity law follows the form

$$v(r) = v_\infty \left(1 - \frac{br_0}{r}\right)^\beta$$

$$b = 1 - (v_0/v_\infty)^{\frac{1}{\beta}} \quad (1)$$

with v_0 the velocity at radius r_0 (usually the minimum velocity at $r_0 = R_*$, but see below).

- The inner atmosphere (photosphere) is in (pseudo-) hydrostatic equilibrium with a velocity law following from the equation of continuity.
- Both parts of the atmosphere are connected at a “transition point” in the sonic region.
- The temperature structure and the continuum radiative acceleration are approximated (since we want to avoid any time-consuming iteration process to establish perfect radiative equilibrium), but nevertheless attain a high degree of precision (see below).
- The spherical extension of the *photosphere* is accounted for.

The advantages of this concept (e.g., compared to the simplified approaches by Hamann & Schmutz 1987 or Hillier 1989) are firstly that we are able to choose *any* value of β without running into methodical problems (such as a transition point lying well above the sonic region or the impossibility of calculating deep into the photosphere). Secondly, due to the almost “exact” treatment of the deeper photosphere (with a radially dependent scale height and not a constant value), a smooth transition to the results of the standard treatment by means of hydrostatic plane-parallel models is enabled in the case of thin winds. Most important, however, is that this method allows us to calculate

wind lines and photospheric lines in parallel with the same degree of precision, independent of the strength of the wind.

Our concept is based on the fact that the Rosseland opacity χ_R (for not too small optical depths, say $\tau_R \gtrsim 0.1$), can be parameterized extremely well by a Kramer’s like opacity formula, which for our purposes can be written as

$$\chi_R(r) \approx s_E(r)\rho(r) \left(1 + k_c \rho(r) T(r)^{-x}\right) \quad (2)$$

where ρ is the density, T is the electron temperature, s_E is the Thomson scattering opacity per unit mass, and k_c and x are fit-parameters which are found from a least squares fit to the Rosseland opacities as function of depth. Note that for small densities this expression reaches the correct asymptotic value of pure electron scattering, independent of the actual fit parameters. Our whole procedure consists now of the iteration of the dependence of the hydrodynamical structure on (k_c, x) (see below), the calculation of new Rosseland opacities based on this stratification, new parameterization, new structure and so on. This process converges typically after six to seven iterations, to the required precision of at least 10^{-5} .

In order to set up the hydrodynamical structure of the atmosphere, we proceed as follows. First, we specify the outer wind according to Eq. 1 and the equation of continuity, where the transition point is prespecified at $v_0 = v(r_0) = 0.1a(r_0)$ (a the isothermal sound speed, which varies with electron temperature T and mean atomic weight $(\mu(r)m_H)$ as $a^2(r) = c_1(r)T(r)$, $c_1(r) = k_B/(\mu(r)m_H)$; k_B is the Boltzmann constant). This turned out to be a reasonable value for all cases considered, which on the one hand results in a smooth transition between wind and photosphere and on the other hand is small enough to justify the neglect of the advection term and the line acceleration in the equation of motion.

With the additional approximation of replacing the flux mean opacity by the Rosseland opacity, we then have

$$\frac{dp}{dm} = g(r) - g_{\text{rad}}(r) = g_* \left(\frac{R_*}{r}\right)^2 - \frac{4\pi}{c\rho(r)} \chi_R(r) H_* \left(\frac{R_*}{r}\right)^2, \quad (3)$$

where $dm = -\rho(r)dr$ is the increment in column density, $p = a^2(r)\rho(r)$ the pressure, and g_* and $H_* = \sigma_B T_{\text{eff}}^4 / (4\pi)$ the gravity and Eddington flux at R_* , which will be defined below. With respect to our parameterization of χ_R , we thus find the first two differential equations governing the photospheric structure by

$$\frac{dp}{dm} = g_* \left(\frac{R_*}{r}\right)^2 - \frac{\sigma_B T_{\text{eff}}^4}{c} \left(\frac{R_*}{r}\right)^2 s_E(r) \left(1 + \frac{k_c}{c_1} p T^{-x-1}\right) \quad (4)$$

$$\frac{dr}{dm} = -\frac{c_1 T}{p}. \quad (5)$$

The boundary conditions for p , T and $r = r_0$ follow directly from the above specified wind conditions at the transition point, and the column density m_0 can be calculated analytically as a function of β and b (cf. also Puls et al. 1996, Appendix A)

$$m_0 = \frac{\dot{M}}{4\pi r_0 v_\infty} h_1(b, \beta) \quad (6)$$

$$h_1 = \begin{cases} -\frac{1}{b} \ln(1 - b), & \beta = 1 \\ \frac{1}{b} \frac{1}{1-\beta} \left[1 - \left(\frac{v_0}{v_\infty}\right)^{\frac{1-\beta}{\beta}} \right], & \beta \neq 1 \end{cases}$$

Finally, we have to specify the temperature stratification. Here, we apply the concept of “NLTE Hopf functions” defined in analogy to the usual Hopf function for the grey case (Mihalas 1978, Sects. 3.3 to 3.4 and references therein), however using the “exact” run of $T(\tau_R)$ from a converged NLTE-model

$$q_N(\tau_R) = \frac{4}{3} \left(\frac{T(\tau_R)}{T_{\text{eff}}}\right)^4 - \tau_R \quad (7)$$

in order to simulate the NLTE effects under the constraint of radiative equilibrium as close as possible. We use our Munich database of hydrostatic plane-parallel NLTE model atmospheres to derive parameterized $q_N(\tau_R)$ -functions, where the principal functional dependence is consistent with the run of the Hopf function for the grey case. Details and examples are given in Appendix B.

We stress that this method and its successful application (see below) relies completely on the fact that the primary depth scale which controls the temperature run is the τ_R scale.

Since the derived q_N -function is taken from a plane-parallel model, we have to consider the additional effects of sphericity, if present in the photosphere, which have been neglected so far. As shown in appendix C, this can be done – at least to a good approximation – by writing

$$T^4(r) = T_{\text{eff}}^4 \frac{3}{4} (\tau'_R + q'_N(\tau'_R)), \quad (8)$$

where τ'_R is the spherical generalization of τ_R and $q'_N(\tau'_R)$ is defined by

$$\begin{aligned} q'_N(\tau'_R) &:= \frac{\tau'_R}{\tau_R} q_N(\tau_R) \\ d\tau'_R &= \chi_R(r) \left(\frac{R_*}{r}\right)^2 dr. \end{aligned} \quad (9)$$

In our model, Eq. 9 is also used to define the stellar radius R_* via

$$\tau'_R(r = R_*) = \frac{2}{3}, \quad (10)$$

which together with the definition of $r_0 = r(v_0)$ specifies all required length scales. Note that in the case of no photospheric extension, Eq. 8 is consistent with the plane-parallel definition. For extended photospheres, however (and assuming the typical situation $r_0 > R_*$), the temperature gradient $dT/d\tau_R$ is smaller for small τ_R and larger for large τ_R , compared to the plane-parallel case.

Neglecting now the depth dependence of the (spherically modified) q-function, it follows that

$$\frac{dT^4}{d\tau'_R} \approx \frac{3}{4} T_{\text{eff}}^4, \quad (11)$$

and the mass variation of τ_R^l is given by

$$\frac{d\tau_R^l}{dm} = \frac{\chi_R}{\rho} \left(\frac{R_*}{r} \right)^2. \quad (12)$$

Thus, the differential equation controlling the temperature reads

$$\frac{dT}{dm} = \frac{3}{16} \left(\frac{R_*}{r} \right)^2 \left(\frac{T_{\text{eff}}}{T} \right)^3 T_{\text{eff}} s_E(r) \left(1 + \frac{k_c}{c_1} p T^{-x-1} \right). \quad (13)$$

Eq. (13) is finally solved in parallel with Eqs. 4, 5 by the Runge-Kutta method to yield the photospheric stratification of $p(m)$, $\rho(m)$ and $r(m)$ for $m > m_0$. Note, however, that after each iteration step the temperature structure itself (in contrast to its use in Eqs. 4, 5 and 13 via assumption Eq. 11) and thus the Rosseland opacity parameters (k_c, x) are calculated from the updated Rosseland depth scale and account for the full depth dependence. For $m < m_0$, the atmospheric structure is obtained from the “wind equation” (1) and Eqs. 8 and 9, together with Eq. 16 (see below). Thus, after converging the whole procedure (i.e., when the Rosseland opacity parameters have stabilized), the complete atmospheric structure is specified. The only obvious inconsistency appears from the fact that our τ_R -scale is based on LTE opacities (since we are just in the starting phase of our calculations and no NLTE values are available), whereas the applied NLTE Hopf function is actually calculated from NLTE Rosseland depths. For a discussion of this problem, see Appendix B and Sect. 3.1.

2.3. Solution of the Rate Equations

Since the solution of the NLTE rate equations is straightforward and documented in standard textbooks (e.g., Mihalas 1978), we will itemize here only the essential features of our code. For the different possible transitions accounted for in the rate equations, cf. Sect. 2.1.

Continuum transport.

- Feautrier scheme in p-z geometry to calculate Eddington factors, iterated with spherical moments equations.
- Boundary conditions: diffusion approximation (lower) and 3rd order (upper boundary)(cf. Auer 1976).
- *Local* approximate Lambda operator (ALO); in our code, we calculate the ALO consistently with the *moments equations* (solving for the diagonal of the inverse of a tridiagonal matrix, see Appendix A in Rybicki & Hummer 1991).

Line transfer.

1. *Either* Sobolev approximation with continuum (Hummer & Rybicki 1985; Puls & Hummer 1988)
 - in cases of stronger continuum than line opacity, $\chi_c/(\chi_l \Delta \nu_{\text{Dop}}) > 1$, the so-called “U-function” is calculated from the extended tables developed by Taresch & Puls (Taresch 1991, see also Taresch et al. 1996).
 - *Local* ALO: $1 - P(r)$ with local (Sobolev) escape probability $P(r)$ (cf. Puls 1991).

2. *or* comoving frame transport (e.g., Mihalas, Kunasz & Hummer 1975).

- As is common, also our approach considers only Doppler broadening when calculating the (line) scattering integrals required for the bound-bound rates. As long as the final formal integral (see below) accounts correctly for the actual broadening (e.g., Stark broadening), this has a negligible effect on the resulting line profiles (cf. Hamann 1981 and Lamers et al. 1987).
- *Local* ALO from Puls (1991)

Coupling of rate equations with radiation transfer: Accelerated Lambda iteration (ALI) with local ALOs from above. For line transfer in the Sobolev approximation, this is equivalent to the reduced rate equation formulation first presented by Klein & Castor 1978 (see also Gabler et al. 1989 and Puls 1991). Our formulation of the photoionization and recombination integrals in the framework of ALI – which differs in a number of aspects from the usual approach – is discussed in Appendix D.

2.4. “Formal Integral”

In order to calculate the emergent profiles, one finally has to solve the formal integral with opacities and emissivities from the converged model. Our solution algorithm has the following features

- Solution on a radial micro-grid
- Separation between line and continuum transport
- Stark broadening
- Consistent treatment of (non-coherent) electron scattering, if required

In the following, we will comment on these different topics.

2.4.1. Solution on a radial micro-grid and separation of line and continuum transfer

The solution of the formal integral (in the observer’s frame) is complicated by the different scales which have to be treated correctly. On the one hand, we have the line processes which act only inside the resonance zones, i.e., on a radial (and frequential) “micro-grid” (cf. Rybicki & Hummer 1978). On the other hand, we have the continuum processes which act on length scales that comprise the complete atmosphere. In order to account for both scales and obtain effective solution algorithms, a number of different approaches have been suggested. Examples are iterative (shooting) methods aiming at improving the radial resolution of the resonance zones (e.g., Hamann 1981), predictor methods aiming at defining the appropriate integration width dz in advance (Puls & Pauldrach 1990), etc..

We have decided to treat the different processes on a radial micro-grid with a typical resolution corresponding to a certain fraction of the thermal Doppler width (say, $v_{\text{Dop}}/5$) or even smaller in the quasi-hydrostatic part of the atmosphere. This approach, when combined with the separation of line and continuum transfer, has the unbeatable advantage that the formal

integral inside the resonance zones can be calculated directly without any additional operations, i.e., essentially by summing up the required quantities. Since we separate line and continuum transfer, outside the resonance zones (which is then the largest part of the atmosphere) almost nothing has to be done, as is shown in Appendix E.

2.4.2. Stark broadening

The calculation of the Stark profiles involves an extensive use of perturbation techniques in the framework of quantum mechanics. A number of authors have performed such calculations for different ions, and we refer the reader to Appendix A for the specific theories we apply in our code. Clearly, Stark and Doppler broadening are present simultaneously in the plasma, and both effects have to be taken into account when calculating the total line profile (the effect of collisional broadening is of minor importance because of the large Stark wings, and can be neglected). Because of their independence, the global profile turns out to be the convolution of the gaussian and Stark profiles, which has been implemented in the corresponding tables.

Typically, Stark broadening for hydrogen and HeII becomes dominant for $\log n_e > 12$. However, to be on the safe side, we switch it on for $\log n_e > 10.5$, whereas for lower densities we account only for Doppler broadening.

2.4.3. Electron scattering

The consistent treatment of electron scattering in the process of line formation leads to the following two effects:

1. Line photons which are emitted in the atmosphere are redshifted by the accumulated effects of electron scattering in the expanding wind. Consequently, the resulting line profiles exhibit an extended red wing, which, e.g. are observed in the emission lines of WR stars (for a detailed discussion of this process, see Auer & van Blerkom 1972). The comparison of calculated and observed scattering wings (if present, which requires a substantial e^- –optical depth and thus a high mass-loss rate) gives valuable information on wind inhomogeneities (cf. Hillier 1991). This process occurs independently of the assumed frequential redistribution, i.e., also in cases of coherent scattering.
2. Due to the significant difference between the thermal velocities of electrons and ions (\sim factor 50 for protons), (line) photons scattered by electrons can be significantly redistributed (by some hundred Å) in frequency. In contrast to the above case which leads to a profile asymmetry (because of the monotonic expansion), this process yields extended wings on *both sides* of the profile. Rybicki & Hummer (1994) have presented a very elegant method to account for this redistribution (which we apply in our code) and discuss the consequences for the emergent fluxes, which are also present at continuum edges. To operate efficiently, however, non-coherent scattering requires a substantial photon injection rate below an e^- –scattering sphere with considerable optical depth. This effect is most probably observed

in the wings of H_α in AB-type supergiants (cf. Kaufer et al. 1996; McCarthy et al. 1995) with low terminal velocity.

In our formal solution package, we have implemented now the consistent treatment of non-coherent e^- –scattering in a way analogous to Hillier (1984, see also Hillier 1991). For a given line source function (from our NLTE code), we recalculate a new continuum source function by iteratively updating the (now frequency dependent) Thomson emissivity in the comoving frame

$$j(\nu) = n_e \sigma_e E(\nu). \quad (14)$$

The e^- –scattering integral

$$E(\nu) = \int_0^\infty R(\nu, \nu') J(\nu') d\nu' \quad (15)$$

(all quantities in the CMF) and the redistribution function $R(\nu, \nu')$ itself (with dipole phase function), however, are calculated as described by Rybicki & Hummer. The converged continuum source function (with e^- –emissivity j) is then interpolated on the appropriate “interaction” frequencies appearing in the formal integral, which is finally computed (cf. Appendix E).

One caveat pointed out to us by W. Schmutz has to be mentioned concerning the above approach. Since we are modifying the electron-scattering contribution while keeping the “true” continuum processes and especially the occupation numbers responsible for the line formation fixed, it is in principle possible that the new continuum radiation field may influence the occupation numbers and hence the whole line. This effect is not accounted for in our present simulations and has to be carefully checked in future calculations by including the effects of non-coherent e^- –scattering in the NLTE code in those cases, when the continuum radiation field is strongly modified.

3. Test of the code

3.1. Atmospheric structure: some results and comparison to plane-parallel models

In the following subsection, we discuss some basic features of our atmospheric models (with special regard to sphericity effects in the photosphere) and compare them to plane-parallel results.

For this purpose and in order to demonstrate the capability of our approach, we have chosen two stellar models at opposite sides of the spectral range we want to address with these kind of calculations, namely a typical O5 dwarf and an A0 supergiant. For details and model names, cf. Tab. 1.

Figs. 1 and 2 compare the run of temperature and electron density of our O-star model with corresponding plane-parallel results. As is obvious, the agreement in the photospheric region is perfect. Note that the temperature structure has been adapted by means of the NLTE Hopf function in such a way as to ensure agreement only until the temperature minimum is reached. The rise to its final value at small τ – which has its origin in the overpopulation of the hydrogen ground state in those

Table 1. Stellar and wind parameters of discussed models. T_{eff} in K, R_* in R_{\odot} , \dot{M} in M_{\odot}/yr , v_{∞} in km/s, $Y = N_{\text{He}}/N_{\text{H}}$, pressure scale height H in percent of R_* and maximum error in flux conservation in percent.

model	T_{eff}	$\log g$	Y	R_*	$\log \dot{M}$	v_{∞}	β	Γ_e	H	r_0/R_*	$\Delta F/F$
OP1	50000	4.0	0.1					0.40			
OW1				18.6	-10.0	1750.	.75		0.09	1.011	1.53
OP2	40000	4.0	0.1					0.17			
OW2				10.	-10.0	2000.	1.		0.1	1.01	3.67
OW3					-6.0					1.003	4.66
BP1	25000	3.0	0.1					0.23			
BW1				30.	-10.0	1300.	1.25		0.2	1.022	1.90
BW2		2.7			-6.30			0.46	0.6	1.023	2.70
BW3		2.7			-5.53					1.013	4.40
AP1	9500	1.5	0.1					0.14			
AW1				100.	-10.0	200.	1.		0.6	1.066	1.67
AW2					-6.0					1.018	2.36
AW3					-5.0					1.0002	6.10
AW4					-4.6					0.952	10.0
AW5					-4.3					0.827	11.2
AW6	9500	1.25	0.1	100.	-10.0	200.	1.	0.25	1.3	1.14	3.9
AP7	9500	0.9	0.1					0.55			
AW7				100.	-10.0	200.	1.		4.7	1.81	10.5
AW8							2.5			1.82	10.0

regions (Auer & Mihalas 1972, Kudritzki 1979) – has been neglected, however. The reason for this procedure is two-fold. At first, the run of the outer temperature is strongly dependent on the specific elements accounted for in the NLTE models (e.g., Werner 1992 and Dreizler & Werner 1992) and in any case is additionally modified by wind-blanketing (Abbott & Hummer 1985; Schaerer & Schmutz 1994), adiabatic cooling (Drew 1989, Gabler 1991) and non-thermal processes (Owocki et al. 1988, Feldmeier 1995). Hence, as long as no final conclusion has been reached, the outer temperature stratification remains somewhat uncertain. On the other hand and fortunately, however, this uncertainty has almost no influence on the resulting fluxes and line profiles, since it affects only layers at small $\tau_{\text{R}} \lesssim 0.01$, where the occupation numbers for the line transitions in question depend on the radiation field mostly and are almost independent on the local temperature. Thus, for our present purpose we have decided to simply neglect the problem and restrict the temperature stratification to a minimum value of

$$T_{\text{min}} = 0.75T_{\text{eff}}, \quad (16)$$

which is typical for plane-parallel NLTE H/He models of almost any spectral type between O and A. The flux conservation that is finally achieved by our procedure will be discussed in detail below.

As is also obvious from Fig. 2, sphericity plays no role for this model, since the pressure scale height

$$H \approx \frac{a^2(T_{\text{eff}})}{g(1 - \Gamma_e)} \quad (17)$$

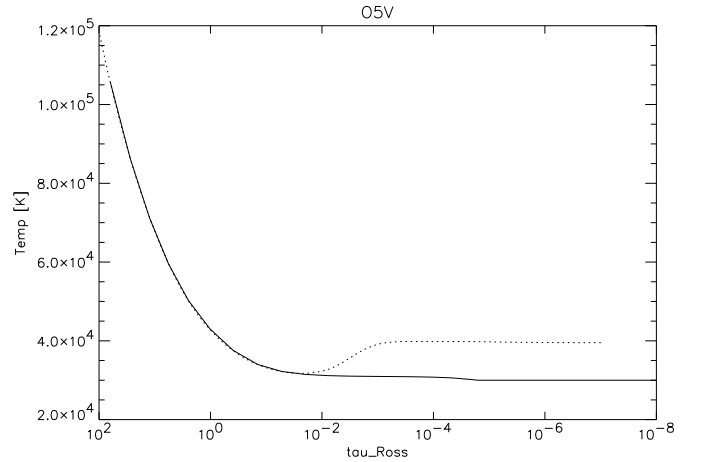


Fig. 1. Comparison of temperatures: O-star model with thin wind (OW2, fully drawn) and corresponding plane-parallel model (OP2, dotted).

(where Γ_e is the ratio of Thomson acceleration to gravity) and consequently the length Δr , from the continuum to the line forming region,

$$\frac{\Delta r}{R_*} \approx \frac{H}{R_*} \ln \frac{m_{\text{cont}}}{m_{\text{line}}} \approx \frac{H}{R_*} \ln(100) \quad (18)$$

is too small (cf. Table 1) to lead to a significant influence. Consequently, the presence of a (moderate) wind affects only the optical depth scale and shifts the transition point to higher τ_{R}

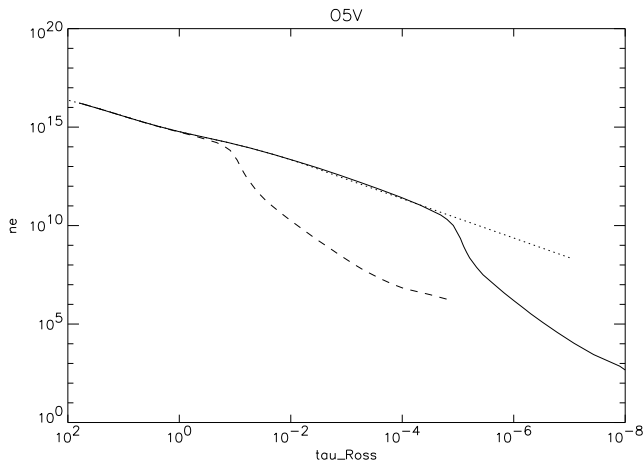


Fig. 2. Comparison of electron densities: O-star model with thin (OW2, fully drawn) and moderate wind (OW3, dashed); dotted: corresponding plane-parallel model (OP2).

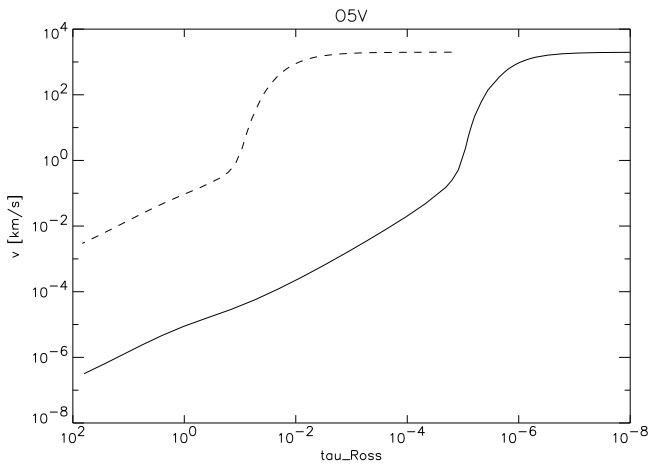


Fig. 3. Velocity fields: O-star model with thin (OW2, fully drawn) and moderate wind (OW3, dashed).

(see also the velocity stratification displayed in Fig. 3), whereas the difference in radius between R_* and r_0 remains small.

This situation changes drastically if we either increase the mass-loss rate in such a way that the optical depth in the wind becomes larger or if the stellar model is put close to the Eddington limit. For the example of an A0 supergiant, both effects are demonstrated in Fig. 4 and Fig. 5, respectively.

In Fig. 4 we have plotted the run of the stellar radius (in units of R_* as function of τ_R for different \dot{M} , ranging from very thin (AW1) to very thick (AW5) winds. As the wind density increases, the location of the stellar radius defined by $R_* = r(\tau_R' = 2/3)$ is shifted more and more into the wind, and the ratio of r_0/R_* becomes smaller and smaller. In this figure, we have denoted the location of the nominal radius, R_* , by squares. For increasing \dot{M} , this location lies at increasing τ_R , since due to the spherical dilution included in Eq. 9, the ratio

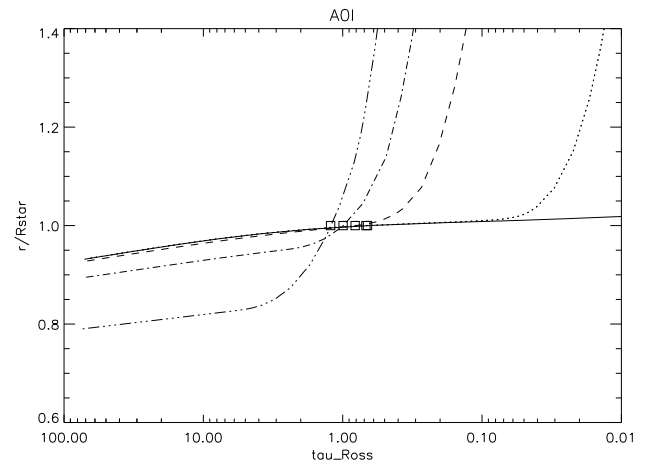


Fig. 4. The mass loss effect: A-star models with thin (AW1, fully drawn), moderate (AW2, dotted), strong (AW3, dashed, AW4, dashed-dotted) and very strong wind (AW5, dashed-triple dotted). The location where the nominal radius $R_* = r(\tau_R' = 2/3)$ is reached for each model is indicated by squares.

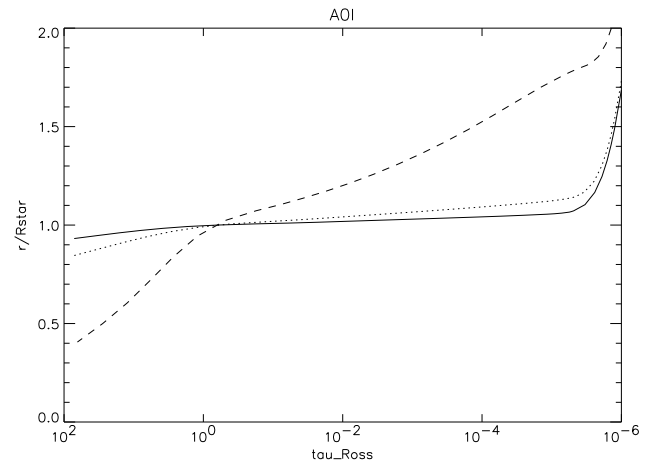


Fig. 5. The scale height effect: A-star models with thin winds and $\Gamma_e = 0.14$ (AW1, fully drawn), $\Gamma_e = 0.25$ (AW6, dotted) and $\Gamma_e = 0.55$ (AW7, dashed). Note the significant expansion of both the lower and the upper photosphere in AW7.

of τ_R/τ_R' is always larger than unity for $r \geq R_*$ and increases with wind density. Note that for very strong winds the lower atmosphere is located at much smaller radii than the nominal radius, a situation familiar from WR-winds. For these models then, the radial difference between line and continuum forming regions is enormous, but originates from the presence of a wind and not from an extended photosphere.

In contrast, Fig. 5 shows just this extension when the gravity is varied in such a way that Γ_e increases from 0.14 (AW1) to 0.25 (AW6) to 0.55 (AW7, AW8) and the wind remains thin (which is, of course, only an artificial assumption). Whereas for AW6 the plane-parallel approximation remains valid (Δr

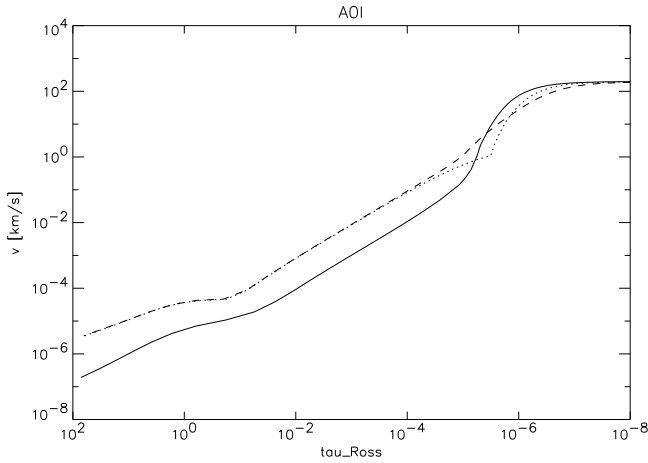


Fig. 6. Behaviour at the transition point between photosphere and wind: A-star models with a thin wind that are far from (AW1, fully drawn, $\beta = 1$) and close to the Eddington-limit (AW7, dotted, $\beta = 1$ and AW8, dashed, $\beta = 2.5$).

(line vs. continuum) $\approx .06R_*$), for our model closest to the Eddington limit (AW7) this difference becomes significant (on the order of 20 %) and will affect both the pressure and the temperature stratification, thus leading to a failure of the plane-parallel assumption. (The obvious change in the slope of r/R_* vs. τ_R at $\tau_R \approx 1$ is due to the onset of the bound-free radiative acceleration.)

Before we further discuss this problem, we want to consider another point related to the velocity- and density stratification, namely the influence of different exponents β . From Fig. 3 (O-star winds with a stellar model of $\Gamma_e = 0.17$) and Fig. 6 (fully drawn curve: A-star wind, $\Gamma_e = 0.14$) we find that the adoption of the typical value $\beta = 1$ usually leads to a smooth transition between wind and photosphere. In those cases, however, where the stellar model lies close to the Eddington limit, this value leads to a significant discontinuity in the velocity gradient (model AW7, dotted). The simple reason for this behaviour is that the gradient of the $\beta = 1$ velocity field is much too steep to match the (outer) photospheric gradient resulting from $dp/dm = g_{\text{eff}} \approx 0$, which occurs for stars close to the Eddington limit due to the rather large bound-free acceleration. In those cases, a smooth transition can be obtained only if the velocity exponent provides a much shallower gradient, e.g. in our model AW8 with $\beta = 2.5$.

Although a bit speculative at present, the requirement of a smooth transition may be the reason that supergiants both of spectral type O (cf. Puls et al. 1996) as well as B-Hypergiants (e.g., P Cygni: Barlow & Cohen 1977, Waters & Wesselius 1986, Pauldrach & Puls 1990) and A-Hypergiants (Stahl et al. 1991) actually show a shallow velocity field with β up to 4 in the most extreme cases.

In Fig. 7 and 8 we now investigate the influence of an extended photosphere. Again, for our A star model far from the Eddington limit both the temperature stratification and the pres-

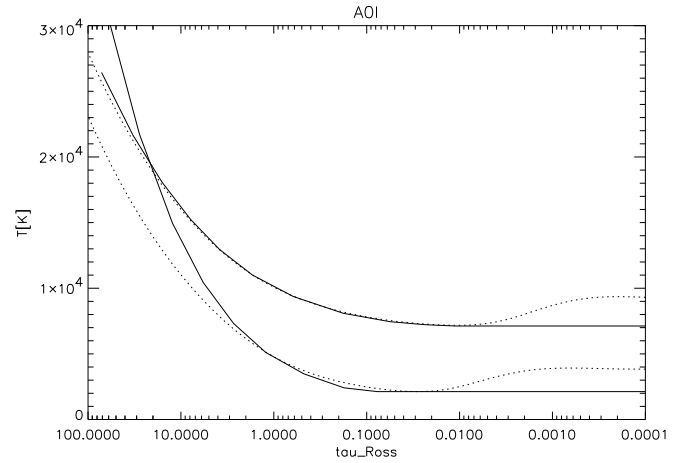


Fig. 7. Temperature stratification – the sphericity effect: A-star model with a thin wind far from the Eddington limit (AW1, upper fully drawn curve) compared to the analogous plane-parallel model (AP1, dotted). Lower fully drawn curve: AW7 (thin wind, close to the Eddington-limit) compared to plane-parallel version (AP 7, dashed). For convenience, both lower curves have been shifted by -5000 K.

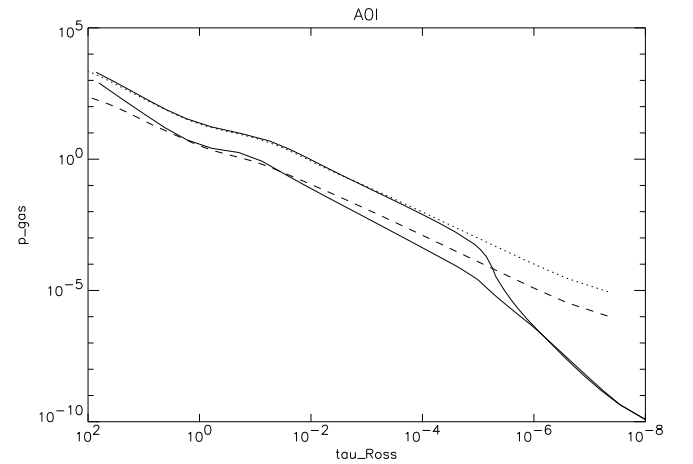


Fig. 8. Pressure stratification – influence of sphericity on gravity and temperature: As Fig. 7, but now for the pressure. (No shift applied)

sure agree completely with the plane-parallel predictions. For our most extreme object, however, the situation is completely different. Here, for $\tau_R \lesssim 1$ the temperature is smaller and for $\tau_R \gtrsim 1$ larger than in the plane-parallel case, and, most importantly, the gradient is very much steeper. This (well-known) result (e.g., Mihalas & Hummer 1974, Gruschinske & Kudritzki 1979) is based on the different τ -scale on which the radiative equilibrium is established, namely on the additional $(R_*/r)^2$ dilution. This strong variation of r with τ_R is also responsible for the different pressure stratification, mostly via the radial dependence of the gravitational acceleration. Thus, the spherical model has a radially dependent pressure gradient throughout the atmosphere, where the pressure is smaller for small τ_R

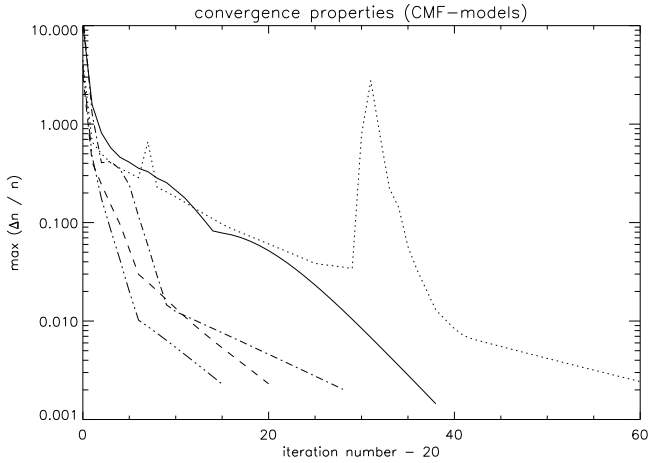


Fig. 9. Convergence properties of CMF-models AW1 (fully drawn), AW8 (dotted), BW1 (dashed), OW2 (dashed-dotted) and OW1 (dashed/triple dotted). Note, that the maximum relative corrections are plotted from the begin of the CMF treatment on, i.e., after the first 20 starting iterations.

and larger elsewhere. Hence, the predictions of a plane-parallel model (which yields a more or less parallel-shift of $\log p$ vs. $\log m$ if the gravity is changed, cf. AP1 and AP7 in Fig. 8) can be substantially altered due to sphericity effects for models close to the Eddington-limit.

In summary, with the described treatment we have a versatile tool at hand which allows us to set up the complete atmospheric structure of massive stars at almost no cost, if we aim at *prescribing* the wind parameters (\dot{M} , v_∞ , β). In our opinion, the only remaining weak point may arise when the NLTE τ_R -scale differs significantly from the LTE scale adopted here. In those cases, which may be present, e.g., in cooler A stars close to the Eddington limit (when hydrogen recombines significantly just in the transition zone), we have to improve our model by introducing an additional iteration cycle to update the structure.

3.2. Convergence properties

In Fig. 9, we have plotted the convergence properties of our (thin wind) models discussed in the next section. In particular, we display the maximum correction (with respect to all levels n and all radii r) $\text{Max}(\Delta n/n)$ obtained as a function of iteration number for our CMF-models OW1/OW2/BW1/AW1/AW8. For convenience, we show these corrections only from the beginning of the CMF-cycle on, which in our treatment starts at iteration number 20. (In order to ensure a fast approach into the convergence radius, we apply 10 pure continuum and 10 Sobolev-transfer iterations before starting with the CMF line treatment.)

In most cases, we achieve a fast convergence rate (mainly controlled by the interplay of the *effective* ground-state continuum and the corresponding resonance (or pseudo resonance) lines) with 15 to 20 iterations necessary per decade of corrections. We regard our models as converged if the maximum

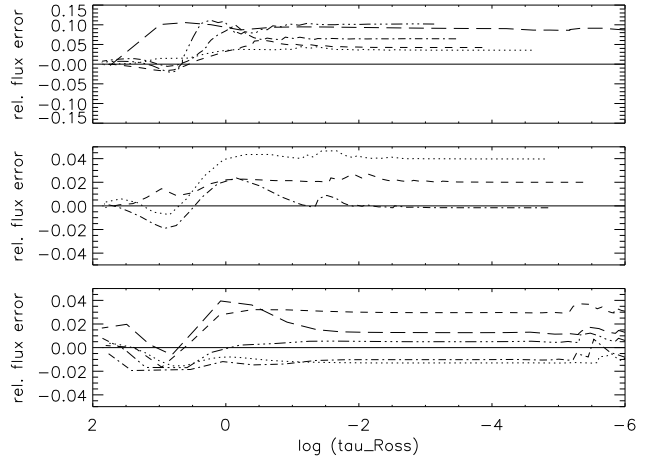


Fig. 10. Error in flux conservation as function of τ_R for the models of Tab. 1. For convenience, the locus of perfect flux conservation is indicated by a fully drawn line. Note the different scalings of the y -axes. Lower panel: (very) thin winds, model OW1(dotted), OW2(dashed), BW1(dashed-dotted), AW1(dashed-triple dotted), AW6(long-dashed). Middle panel: moderate winds, model OW3(dotted), BW2(dashed), AW2(dashed-dotted). Upper panel: dense winds or very extended photosphere, model BW3(dotted), AW3(dashed), AW4(dashed-dotted), AW5(dashed-triple dotted), AW8(long-dashed).

correction lies below 2 per mille, which is sufficient as long as the ALI works reliably.

With this requirement, we need (in total) a typical number of 40 to 60 iterations to converge a model, where the only exceptions occur in cases when the ground-state continuum is extremely thick and the model lies close to the Eddington limit (cf. model AW8 in Fig. 9). In those cases, we may find a stagnation of the convergence process (e.g., at iteration number 30 for AW8). In order to re-accelerate the iteration in those cases, we perform an Aitkins-extrapolation of the problematic (ground-state) occupation numbers, exploiting the fact that the effective eigenvalue controlling the convergence can be derived from three consecutive iterations (e.g., Puls & Herrero 1988, Eq. 21). With this extrapolation (resulting in a “spike” of the maximum correction), we then drive the iteration back into a faster convergence rate.

3.3. Flux conservation

In Fig. 10, we have plotted the relative errors in flux conservation for our wind models from Tab. 1 as a function of τ_R (see also the last column of Tab. 1, which gives the *maximum* flux error). The lower panel displays the case for thin winds, the middle one for moderate winds and the upper one for strong winds and the model with the very extended photosphere, AW8. Except for the latter case, all other models conserve the flux at a 2% level or better for large $\tau_R \gtrsim 10$. The maximum errors occur (as to be expected) near $\tau_R \approx 1$ and remain constant afterwards for the majority of the cases. As is obvious, for all models with

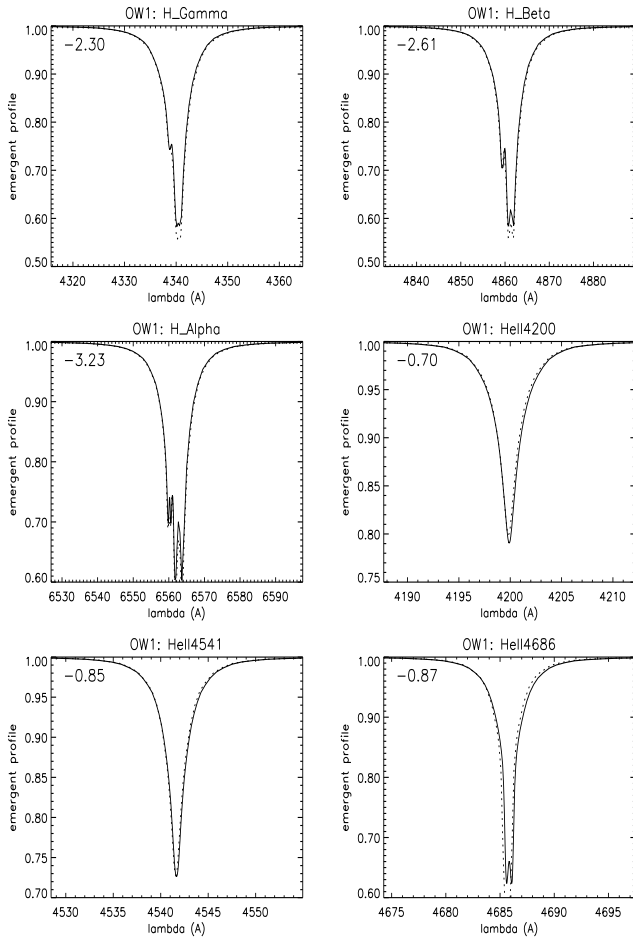


Fig. 11. Comparison of line profiles: strategic hydrogen (incl. bluewards HeII blend) and HeII lines of CMF-model OW1 (fully drawn) vs. plane-parallel results (OP1, dotted). Here and in the following, the number in the upper left corner gives the equivalent width of our profiles in Å, defined as positive for net emission.

not too dense a wind this maximum error lies below 4%, with typical values between 2. . . 3%.

As is also obvious, the flux conservation in cases with a large \dot{M} and/or extended photosphere is far from perfect. There are two reasons for this problem. First, our procedure of translating a plane-parallel temperature stratification into a spherical one (which is decisive in the discussed context) is not exact but only approximate (cf. Appendix C). Second and already outlined above, our temperature stratification is only calculated on the basis of a LTE τ_R scale and should be updated if pronounced NLTE effects contaminate the scale. E.g., the typical depopulation of some important ground states will reduce the background opacity and should not be neglected. Furthermore, this depopulation is different in atmospheres with and without mass-loss (e.g., Gabler et al. 1989) and can lead to additional differences even if the Rossland scale is updated, since our NLTE Hopf-function is derived from plane-parallel models.

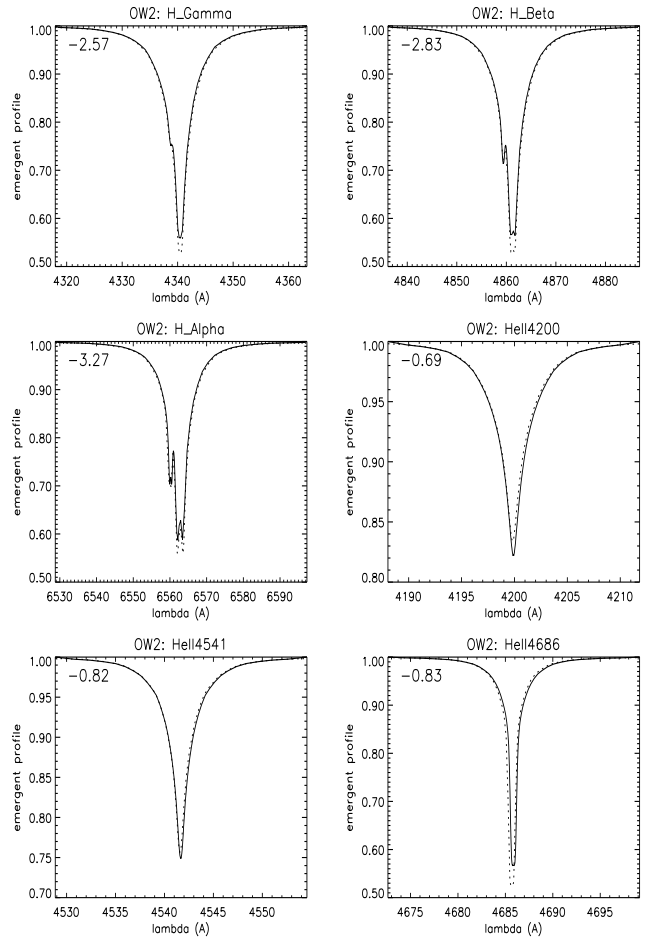


Fig. 12. As Fig. 11, but for model OW2 vs. OP2.

In conclusion, our treatment of defining the temperature stratification leads to satisfying results under not too extreme atmospheric conditions. For the remaining models with a larger discrepancy (with corresponding maximum errors in temperature of order 2.5%), we will not forget the problem and will work on an improved version of the code. However, we point out that the important “photospheric” profiles of those models – in comparison to plane-parallel ones – are much more affected by mass-loss and/or sphericity effects than by the uncertain temperature calibration, so that we consider this problem to be at present of only minor importance.

3.4. Profiles of thin wind models vs. plane-parallel results

One of the major requirements for a reliable (expanding) atmosphere code is that it reproduces the results of plane-parallel calculations in the case of (very) thin winds and non-extended atmospheres. If this requirement is not fulfilled, one would introduce a systematic and maybe important off-set, especially when one analyzes atmospheres with small but non-negligible winds, and compares the results with those from conventional plane-parallel models. An important topic, e.g., which closely

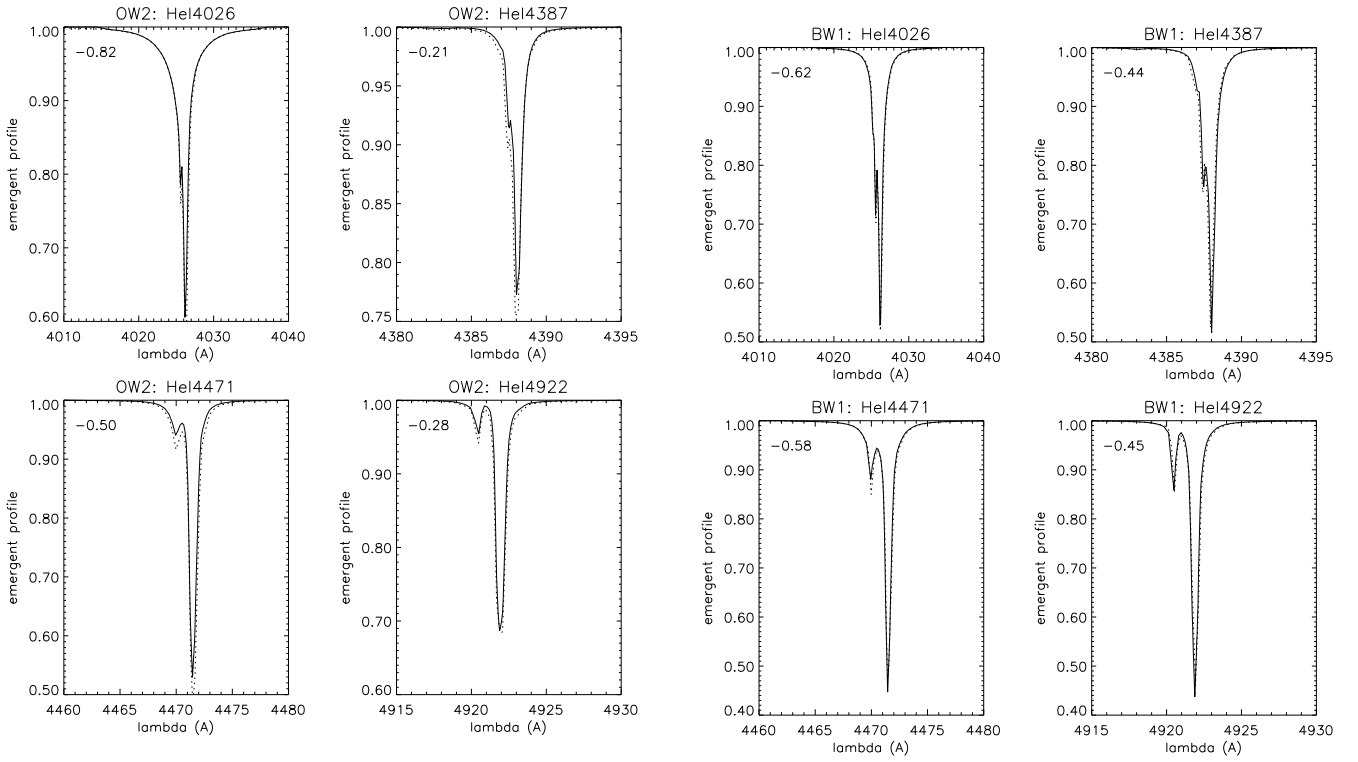


Fig. 13. Comparison of line profiles: He I lines of CMF-model OW2 (fully drawn) vs. plane-parallel results (OP2, dotted). Note, that He I 4026 is dominated by He II 4026 ($4 \rightarrow 13$). The features bluewards from the central ones are the forbidden components of each He I line.

Fig. 15. He I lines of model BW1 and BP1. Here, the contribution of the He II blend to He I 4026 is marginal.

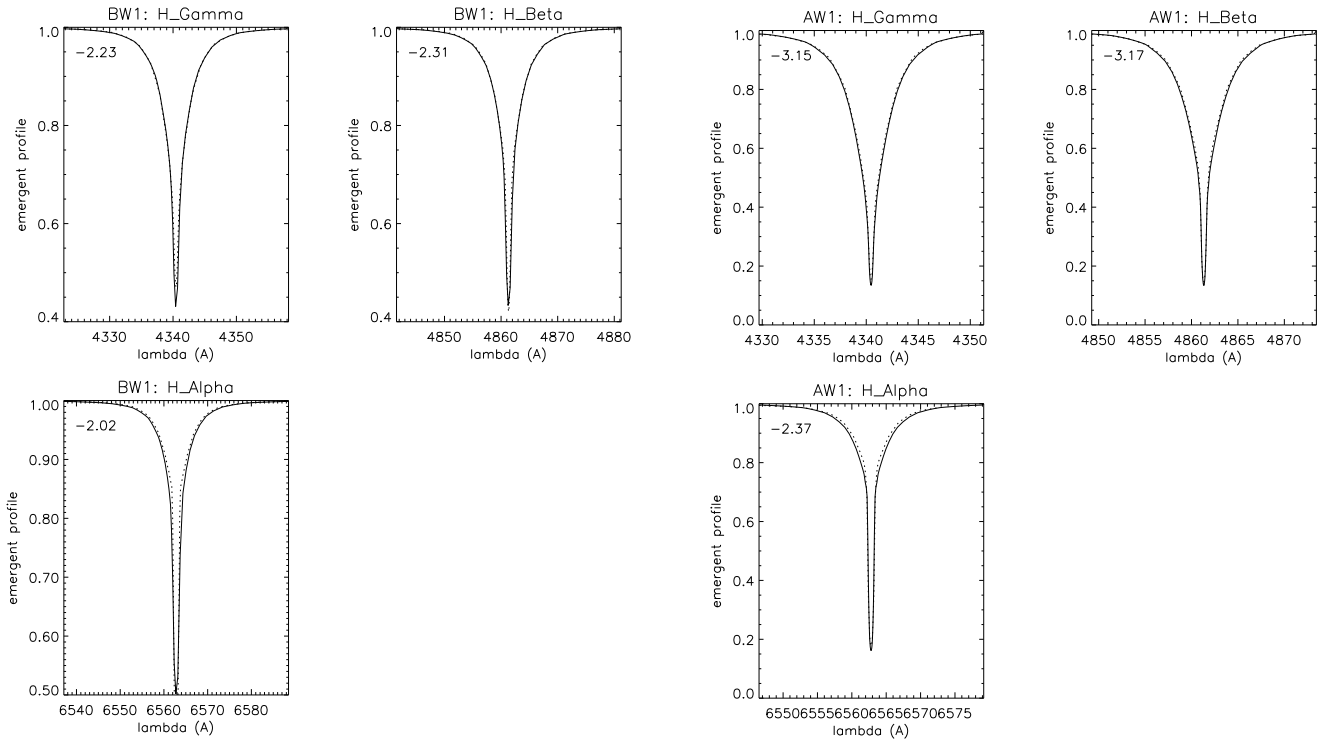


Fig. 14. Hydrogen Balmer lines (incl. He II blend) of model BW1 vs. BP1.

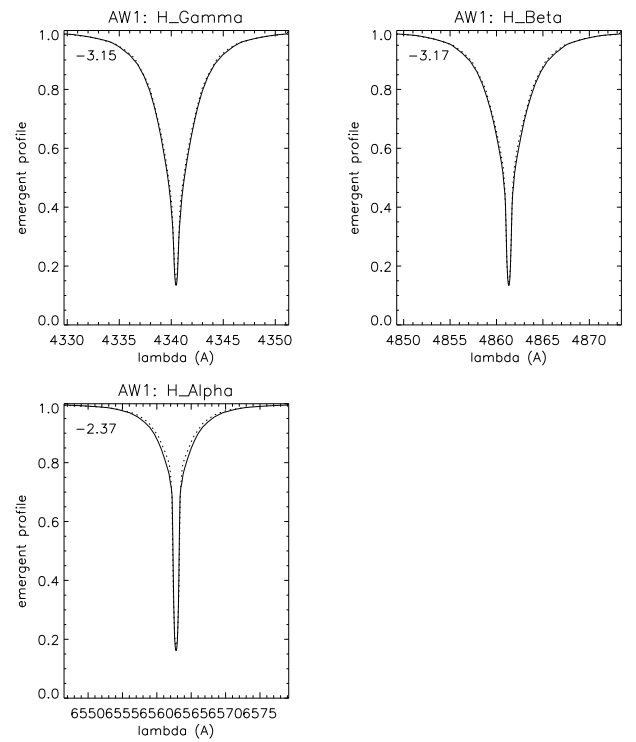


Fig. 16. Hydrogen Balmer lines of model AW1 vs. AP1.

relates to this problem is the comparison of actual and predicted mass-loss rates of stars with thin winds, where one has to be sure that the refilling of a photospheric profile is due to the wind and not due to an inconsistency in the line formation process in the different codes under consideration.

To our knowledge, however, the fulfillment of this important requirement has rarely been demonstrated by the different wind codes on the market, at least not for a wide range of physical conditions. With the following plots (Figs. 11 to 16, T_{eff} ranging from 50,000 to 9,500 K), we want to show that our code has the desired ability. The agreement of our H/He-profiles with the corresponding plane-parallel ones is striking. If present at all, differences are found only in the very line cores and are definitely due to different grid sizes and angular integration methods. In these figures, we have deliberately plotted the purely theoretical profiles without any rotational convolution to emphasize the agreement not only of the major component but also of the minor one, i.e., of the HeII blend in the hydrogen Balmer lines and in HeI 4026 (where the blend dominates in O- and early B-type spectra) and of the forbidden components of all HeI lines.

However, we have also encountered some problems, which are discussed in the next two subsections.

3.4.1. HeI lines in hot O-stars

After having calculated a relatively large grid of models and profiles (from which we have shown only some representative examples), a comparison with the corresponding plane-parallel profiles resulted in the following dilemma: While the hydrogen Balmer and HeII Lyman lines turned out to be in satisfactory agreement throughout the complete model grid, for models with $T_{\text{eff}} > 40,000$ K the HeI lines began to deviate from the plane-parallel solution. The difference grew with temperature, and our profiles were always weaker. Fig. 17 (OW1, $T_{\text{eff}} = 50,000$ K) is a typical example for the problem. We performed our following investigations by means of this model.

At first, we realized that in the corresponding plane-parallel model (OP1) the HeII Lyman lines were in detailed balance almost throughout the complete atmosphere. In our calculation, however, they (i.e., actually the transitions $1 \rightarrow 3, 4, \dots$) left detailed balance in the same region as the ground-state ionization/recombination rates left detailed balance, namely at $\tau_{\text{R}} \approx 0.01$. In a second step, we therefore put these lines artificially into detailed balance (which is very easy to do with a data-driven code!) and actually found a much better agreement with the plane-parallel results (cf. Fig. 18). Since in our model the population of the decisive HeII ground state (all HeI levels are coupled to this state and vary in proportion) was smaller than in the plane-parallel case, whereas especially the HeII($n = 2$) level was in perfect agreement, there was only one possible solution: In all our Lyman-lines, the scattering integrals had to be much higher, thus effectively pumping electrons from the ground state into higher states and depopulating the ($n = 1$) and coupled HeI levels.

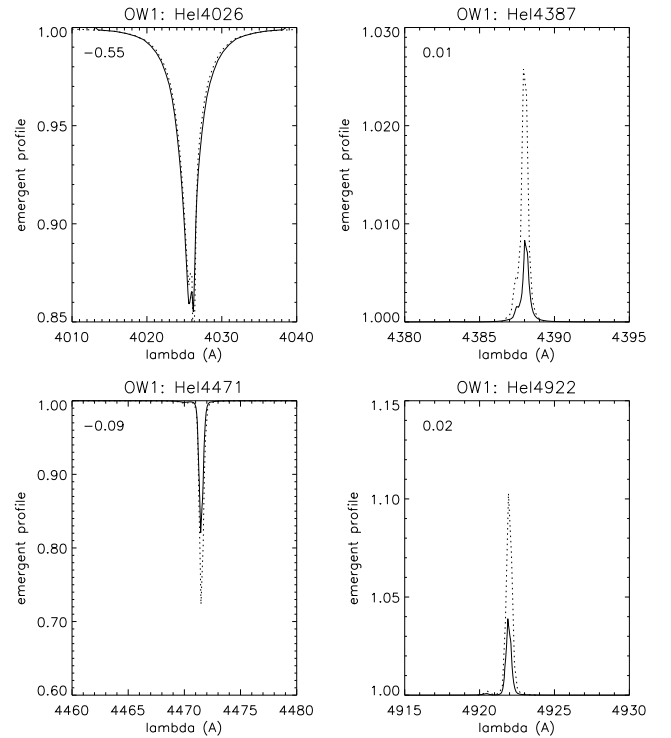


Fig. 17. As Fig. 13, but for model OW1 vs. OP1. For the differences between our (fully drawn) and the plane-parallel solution, see text.

This argument was supported by the fact that all net radiative rates (except of the $(1 \rightarrow 2)$ line, which also in our model is in detailed balance until far out in the atmosphere) of the Lyman lines were negative and dominated the rate equations.

Hence, we sought for a mechanism which enlarged the mean line intensities compared to the plane-parallel calculations. This mechanism was finally found in the different ways both approaches approximate the influence of electron scattering in the NLTE line transfer. (“Approximate”, since at present neither code accounts for the correct electron scattering redistribution function because of computational time limitations.)

On the one hand, the plane-parallel models approximate the Thomson scattering process to be always as *coherent*, $j_{\nu} = n_e \sigma_e J_{\nu}$, even in the lines. In contrast, our approach, as is typical for all available CMF-codes, regards the Thomson emissivity to be constant over the line, with a value taken from the neighbouring continuum, $j_{\nu} = n_e \sigma_e J_{\nu}^{\text{cont}}$. This approach follows from the argument that the electron scattering redistribution function has a much larger frequential width than the line redistribution function (cf. Sect. 2.4.3) and is justified by the investigations of Mihalas, Kunasz & Hummer (1976), who showed that the second approximation (our approach) leads to a much better agreement with the exact solution than the coherent one.

In the “normal” case, this different formulation has only a marginal influence on the results, which is obvious from a comparison of the line profiles we have plotted above. Here,

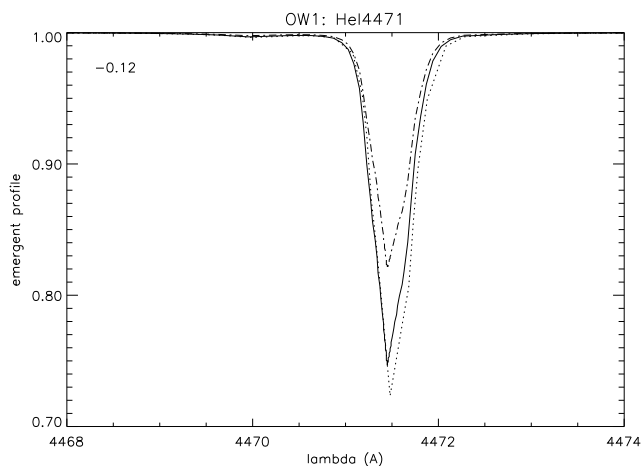


Fig. 18. He I 4471 of CMF model OW1 (dashed-dotted), for the same model, however with He I Lyman lines forced into detailed balance (fully drawn), and for the plane-parallel model OP1 (dotted).

however, the situation is different, since the continuum radiation field at the He I Lyman lines ($229 \text{ \AA} < \lambda < 303 \text{ \AA}$) is extremely hot in pure H/He atmospheres, due to the dominating Thomson scattering background opacity. Typical radiation temperatures are $T_{\text{rad}} \approx 60,000 \text{ K}$ for a $T_{\text{eff}} = 50,000 \text{ K}$ model. Thus, the strong continuum radiation field becomes important, leading to much larger “line” intensities than in the case when Thomson scattering is treated in the coherent approximation. (In the latter case, this term becomes negligible since it is almost completely decoupled from the continuum due to the dependence via the mean *line* intensity J_{ν} .)

In order to check this chain of arguments, we have run a simulation with no Thomson-scattering at all in the He Lyman lines. Actually, we obtained essentially the same results as if the lines were treated in detailed balance, although in the outer but subsonic parts an additional influence of the velocity field was perceptible in the occupation numbers, though not visible in the profiles.

The consequences of this investigation are not especially encouraging, though not completely unexpected. On the one hand and from a standpoint of consistency, our results (in particular the weaker He I 4471 line) seem to be more accurate, since the coherent approximation is more unrealistic than ours. On the other hand, in reality there is a large bound-free background opacity in the spectral region under discussion due to the metal ions neglected in our H/He models, which will drive the radiation temperatures back to much cooler values. Thus, at a first glance the “plane-parallel” result seems more physical. However, first test calculations including line blocking and blanketing (Sellmaier 1996) point to the possibility that a fully consistent treatment of the problem also reduces the strength of the He I ground state and thus of the 4471 line. The effect arises in these models by coupling the Lyman lines strongly to the pseudo-continuum created by the large number of overlapping lines in the EUV, which, since they are scattering dominated,

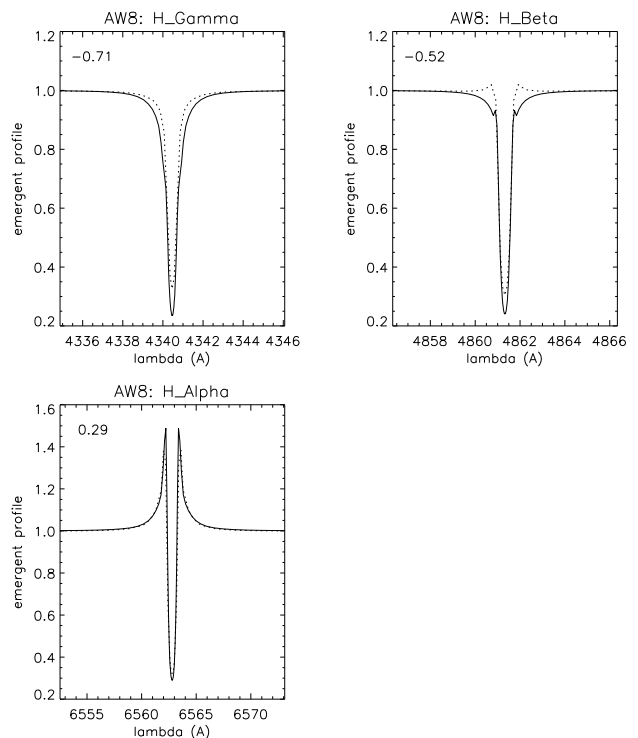


Fig. 19. Hydrogen Balmer lines of model AW8 vs. AP7.

maintain the high radiation temperature characteristics of the Thomson opacity discussed above.

In any case, before the final word can be said about the actual behaviour of He I 4471, which is at present the only temperature indicator of hot O-stars, the absolute temperature scale above 45,000 K (and, consequently, luminosities) derived by this line only should be regarded with caution.

3.4.2. Balmer lines in A-stars close to the Eddington limit

In the last part of this section, we discuss briefly the behaviour of the hydrogen Balmer lines in A-stars close to the Eddington limit, displayed in Fig. 19 (models AW8, AP7). At first, the emission line character of H_{α} (which is not present in the corresponding models with higher gravity (AW1, AP1, Fig. 16) is somewhat puzzling, however it is both theoretically understood (Hubený & Leitherer 1989) and also observed (e.g., Kaufer et al. 1996, McCarthy et al. 1995). Briefly, this emission arises from the fact that the effective $n = 2$ groundstate is depopulated by photoionizations in the Balmer continuum, where the corresponding radiation temperatures and thus the depopulation is stronger for lower gravities. The latter effect is due to the lower pressure and density in models with lower $\log g$, so that the point of $\tau = 1$ in the Balmer continuum is shifted (compared to higher gravity models) inside to higher temperatures.

The differences between our Balmer profiles and those of the plane-parallel models are now readily understood as differences due to the expansion of the photosphere, a phenomenon which is not accounted for the the plane-parallel approxima-

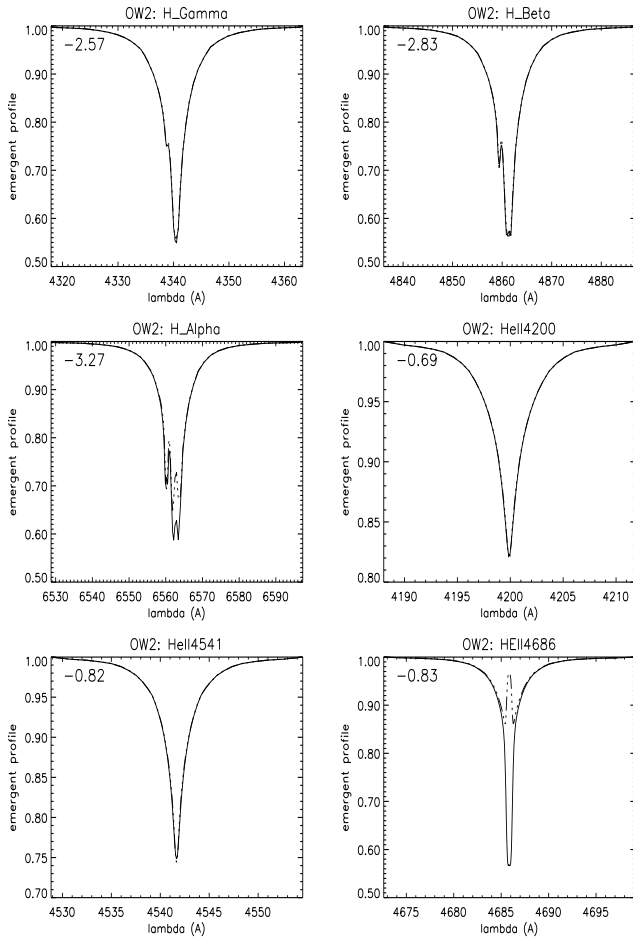


Fig. 20. Hydrogen and HeII profiles from CMF(fully drawn) and Sobolev plus continuum (dashed-dotted) line transfer in the NLTE solution, for model OW2

tion. As already discussed in Sect. 3.1 (cf. Fig. 8), our models have a different run of pressure because of the $g(R_*)R_*^2/r^2$ dependence of the gravity. Consequently, with respect to the formation of the Balmer continuum, our models have a higher effective gravity than the plane-parallel ones in the decisive layers, so that the ($n = 2$) level is not as much depopulated and our profiles display lower emission. This is clearly visible in the H_β and H_γ lines. That the H_α line fits so nicely is more or less by chance and related to the fact that this line is formed further out in the atmosphere than the other two lines. There, because of the likewise different dilution factors, we have an additional influence on the ionizing radiation field and thus an additional difference in the $n = 2$ departure, which partly compensates for the $\log g$ -effect.

Thus, due to the fact that photospheres close to the Eddington limit become extended, the gravity values derived from plane-parallel H_γ lines have to be corrected to even *lower* values.

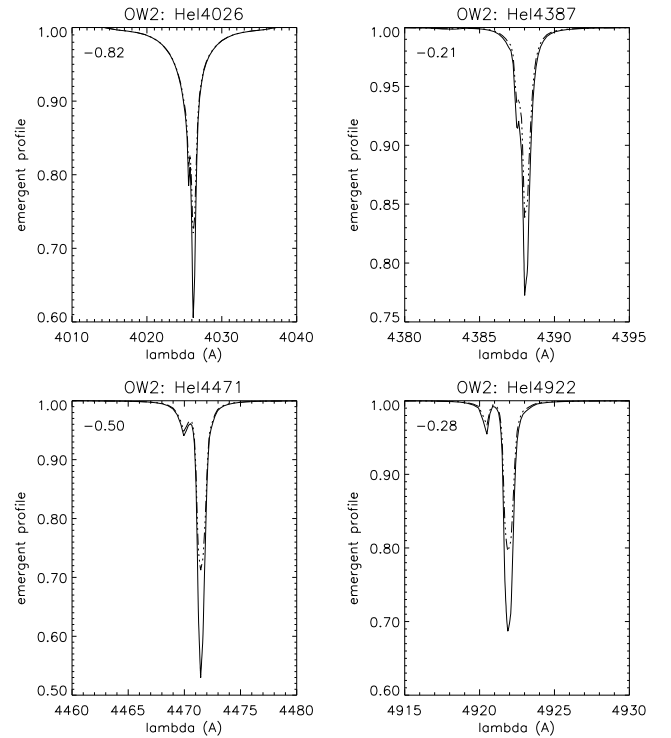


Fig. 21. As Fig. 20, but for HeI lines.

3.5. Comparison of CMF and Sobolev (plus continuum) line transfer

In this section, we will briefly compare the profiles resulting from the two alternative methods of line transfer which we can apply in our NLTE code, namely the CMF- and the Sobolev plus continuum transfer (cf. Sect. 2.3). Since this matter is well discussed in the literature (e.g. Hamann 1981, Gabler et al. 1989, de Koter et al. 1993, Sellmaier et al. 1993), we will address only those points which may deserve some additional statements. Figs. 20 to 23 display the situation for a large number of typical cases, both with respect to temperatures and wind densities as well as for different (strategic) lines. Note, however, that the following remarks apply only *if the temperature stratification remains unaffected by the line transfer method*, i.e., if we use an identical atmospheric model both for CMF and SA transport. If this were not true, we could obtain larger differences since the type of line transfer would then also affect the ionization structure via a different temperature structure resulting from a different adjustment of radiative equilibrium. Our findings can be summarized as follows:

- For all models considered, the line wings – whether they are in absorption or emission – agree perfectly.
- If there are differences at all, these occur only in the line cores, where the SA occupation numbers always generate too much emission.
- An essential *failure* of the SA occurs only for moderate mass-loss rates, whereas the differences for very low and

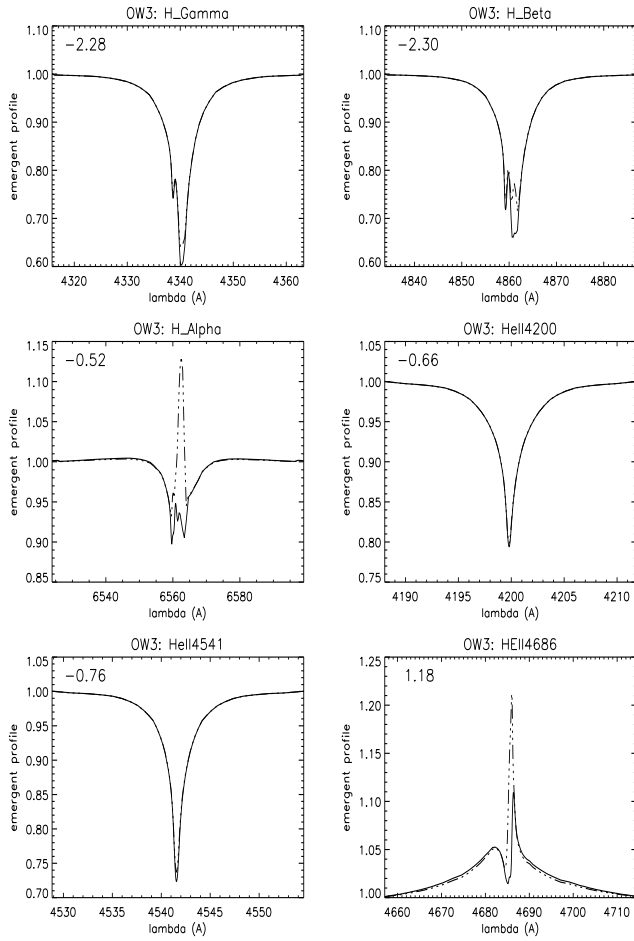


Fig. 22. As Fig. 20, but for model OW3 (moderate wind)

large \dot{M} are acceptable in the framework of atmosphere analysis.

Before we give some theoretical arguments, let us describe the differences of the calculated profiles. Fig. 20 and 21 display the H/He lines for a 40,000 K dwarf with (almost) no wind. A significant discrepancy is only found in the HeII 4686 line, where the line core of the SA model begins to turn into emission. All other lines agree fairly well, although the cores of the HeI lines are too weak. The differences in the equivalent width, however, are only small, typically of the order of 20 to 30 %. This is also true for the other models investigated here, so that we do not present the corresponding HeI profiles explicitly. Note, however, that a consequent use of profiles resulting from SA calculations (which are considerably cheaper with respect to computational time) for atmospheric analyses would create a *systematic* shift to cooler temperatures, compared with conventional plane-parallel methods.

With increasing, but moderate, mass-loss (Fig. 22, model OW3, $\dot{M} = 10^{-6} M_{\odot}/\text{yr}$), H_{α} becomes the most deviating line, with the wings in absorption and the core in emission. With respect to observed H_{α} profiles, this one is of course unrealistic. On the other hand, HeII 4686 has now a full emission profile,

so that the discrepancy becomes marginal when a rotational convolution is performed.

Since the situation for O-stars with higher wind density is discussed extensively in the various papers cited above, and differences are shown to be present only in the weakest, e.g., HeI, lines, we skip this parameter range and proceed to the B-star domain (models BW1 to BW3 at 25,000 K, Fig. 23, upper three panels). Here, the locus of maximum discrepancy migrates with increasing \dot{M} from H_{α} to H_{β} , and would be present in H_{γ} for even stronger mass-loss rates. Note, that H_{α} in BW2 and H_{β} in BW3 have the largest deviations of all models considered in our investigation and would lead to crucial misinterpretations if used uncritically.

The lower three panels of Fig. 23 show the hydrogen Balmer lines for some representative A-stars models (all with $T_{\text{eff}} = 9,500$ K). In the first one (AW1, negligible \dot{M}), all three profiles (being of similar strength) display the same degree of inconsistency, namely the narrow cores are completely refilled in the SA simulation. In contrast, for the model with the largest mass-loss rate discussed here (AW3), not even the slightest difference can be “observed”. Finally, the profiles of the SA model AW8 (the one close to the Eddington limit) show again too much emission in the line cores, so that especially H_{β} would lead to wrong conclusions.

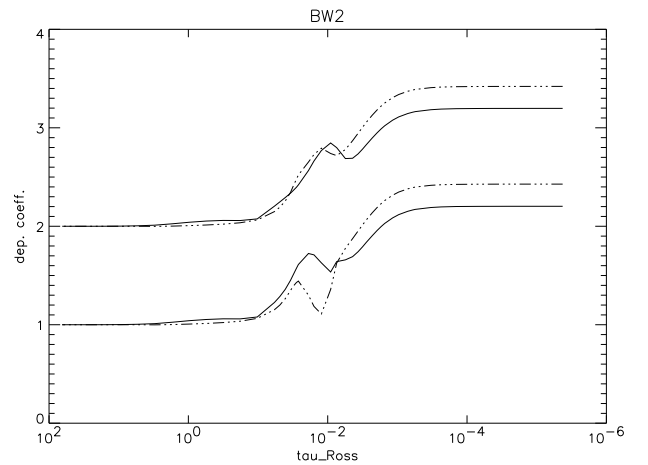


Fig. 24. NLTE departure coefficients of hydrogen, $n = 2$ (fully drawn) and $n = 3$ (dashed-dotted), for model BW2 and CMF line transfer (lower curves) and Sobolev transfer (upper curves). For convenience, both upper curves have been shifted by +1.

The immediate reason for the additional emission in the line cores that occurs with the Sobolev transfer is displayed in Fig. 24. We compare the departure coefficients of the hydrogen $n = 2, 3$ level of model BW2 (with the largest discrepancy in H_{α}), resulting both from the CMF and the SA treatment. Whereas in the continuum forming region and in the wind the agreement is perfect, the difference is considerable at optical depths where the line core is formed, i.e., where the line begins to become optically thick ($\tau_R \gtrsim .01$). Since in the SA

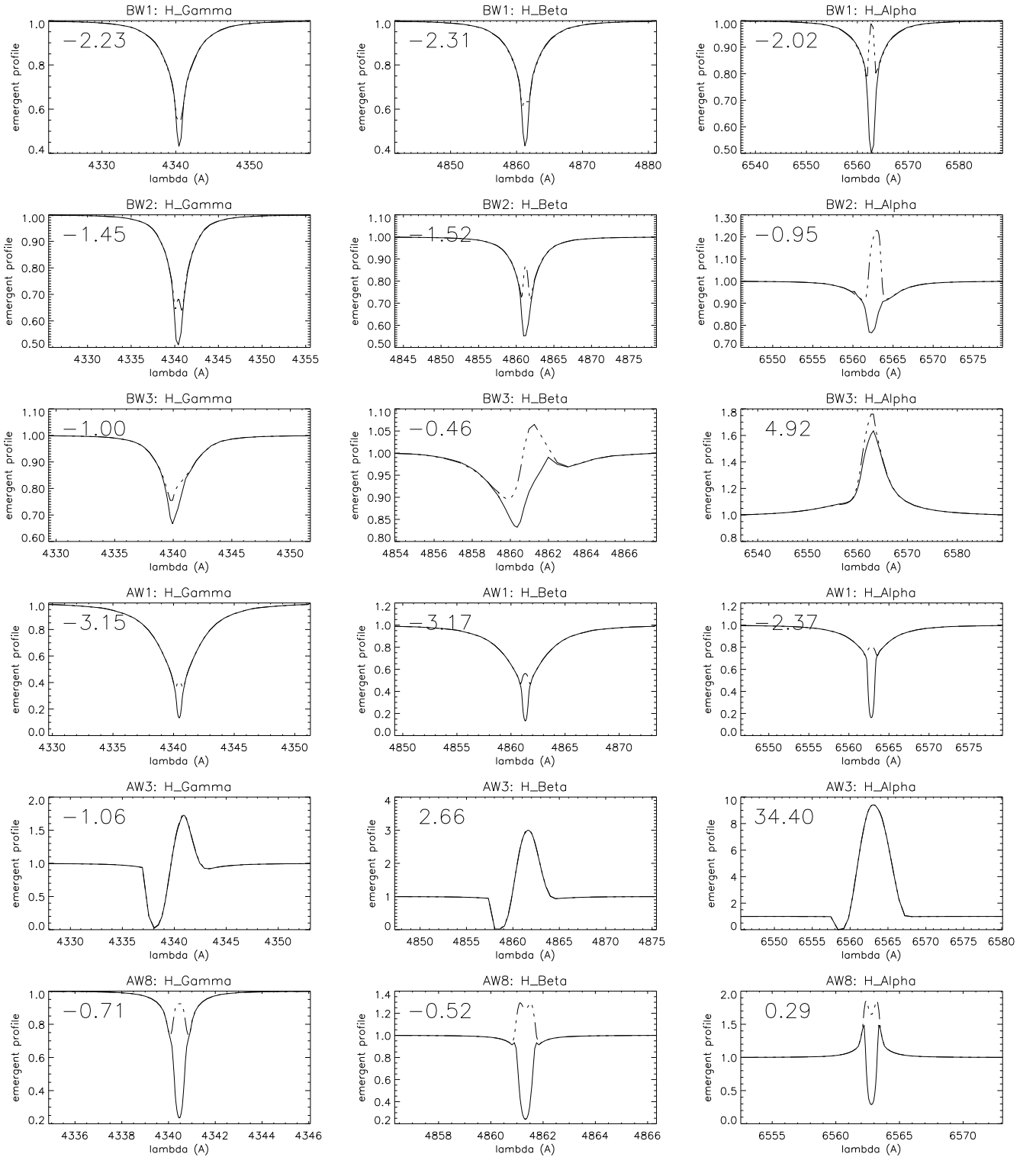


Fig. 23. CMF (fully drawn) vs. Sobolev (dashed-dotted) line transfer for hydrogen Balmer lines. Models BW1(no), BW2(moderate) and BW3(strong wind); AW1(no), AW3(very strong) and AW8(no wind, close to the Eddington limit). Note that the agreement of the profiles in AW3 is so good that the differences, although plotted, are not visible.

simulation the departure coefficient of the upper level is larger than the lower one (and the radiation temperature at H_α is not too different from T_e), it is clear that the line core must appear in emission. The reason that the $n = 3$ level (SA) is more strongly populated than in the CMF case (which is true for the upper levels of all lines showing a discrepancy) was discussed in considerable detail by Sellmaier et al. (1993): particularly for lines that are not too strong, the Sobolev approximation leads to an overestimation of the mean line intensity in the region of the ion's thermal point. This is caused by the fact that the *curvature* of the velocity field in the transition zone is most pronounced, which causes in reality an asymmetric line escape probability for outwards/inwards directed photons. By means of the (conventional) SA, however, the escape probability is taken to be symmetric (only dependent on the local velocity *gradient*) and *underestimates* this quantity. Thus, for lines which are neither completely optically thin nor thick the mean line radiation field becomes too strong, thereby effectively overpopulating the upper levels with respect to the exact CMF solution which accounts for curvature terms appropriately. For this reason, it is always the line that just becomes optically thick in the transition region that shows the largest discrepancy. This explains why the discrepancy is shifted to weaker lines with increasing mass-loss. This also explains why the He I lines in O-stars are not as wrong as one might suspect: Since the only line processes which affect the ionization are the He I resonance lines (cf. Sect. 3.4.1), the overall ionization is correctly treated because these lines remain optically thick (or continuum dominated) much further out in the atmosphere. Thus, the erroneous SA treatment plays almost no role for the establishment of the ionization equilibrium and the differences in the line cores are again due to differences within the He I lines themselves.

4. Summary and future perspectives

We have introduced a new and fast NLTE line formation code as a versatile tool for the spectroscopic analysis of hot stars with winds. We have shown that this code fulfills one of the most stringent requirements for such an objective, namely to reproduce both the photospheric stratification and the line profiles resulting from an alternative plane-parallel treatment in the case of very thin winds. Thus, we are now able to account for wind effects also in lines which are only weakly wind contaminated and avoid the problem of erroneously attributing inconsistent plane-parallel vs. expanding atmosphere results to real physics.

At first glance, the treatment of the wind by means of a prescribed velocity field and mass-loss rate may be regarded as a drawback compared to a consistent treatment including the theory of radiatively driven winds (e.g., the unified model atmosphere concept by Gabler et al. 1989). However, in view of the present uncertainties in the theory, mainly with respect to the “ β -problem” outlined in the introduction and the wind momentum problem (see Lamers & Leitherer 1993 and Puls et al 1996), this procedure provides the maximum degree of freedom for the synthesis of spectra and avoids biased results.

From the thorough tests we have performed in a wide range of spectral class, luminosity and wind density, three points have come to our attention which turned out to be essential for an accurate spectroscopic analysis of blue stars. First, the absolute temperature scale for stars with $T_{\text{eff}} \gtrsim 45,000$ K is uncertain if derived from He I lines alone, since the strength of these lines almost exclusively depends on the behaviour of the He II resonance lines, with all the present uncertainties such as the correct treatment of electron scattering and line-blocking in the spectral region below roughly 310 \AA . Independent methods such as the analysis of the optical N III, IV and V lines or the FUV Ar VII lines (if available, cf. Taresch et al. 1996) will provide an additional check in future temperature calibrations, even if the situation for He I has been clarified.

Second, for stars close to the Eddington limit one has to account for the photospheric extension, since this changes the *slope* of the pressure stratification and all related quantities such as the temperature run. Especially concerning the gravity determination (which is difficult for those objects in any case), this different slope and its consequences for the formation of the line wings can lead to significant changes in comparison to results derived from the plane-parallel approximation.

Finally (and most regrettably), the diagnostics of atmospheres with only moderate wind densities are severely affected by the use of the Sobolev line transfer (even when used in a sophisticated form), as long as the escape probabilities are evaluated by assuming a foreaft symmetry. So far, one must use the “exact” transfer (e.g., CMF) since otherwise at least the inferred mass-loss rates would be *underestimated* due to an inappropriate refilling of the line cores in the SA simulation.

Although with the development (and first applications) of this code we have made significant progress towards the routine quantitative spectroscopy of blue stars with winds, some caveats should be mentioned.

The authors are well aware that the rather simple approach taken here is only the first step towards a realistic description, especially if one plans to analyze metal abundances or tries to use metal lines as indicators of stellar parameters (e.g., silicon for the temperature calibration of B-supergiants). Although the incorporation of the considered elements is easy to manage due to our data-driven input, the correct calculation of the ionization equilibria (especially of trace ions) requires one to account for the EUV line-blocking/-blanketing (cf. Sect. 1) and, if present, the soft X-ray/EUV radiation field (MacFarlane et al. 1993, Pauldrach et al. 1994, MacFarlane et al. 1994) arising from the cooling zones of shocks (Hillier et al. 1993, Feldmeier et al. 1996) generated by line-driven instabilities (Owocki et al. 1988, Feldmeier 1995) and the merging of consecutive shocks (also Feldmeier et al. 1996).

Since particularly the incorporation of an exact treatment of line-blocking is much too time-consuming for the concept outlined here, we will have to rely on approximate methods for calculating the required background opacities, e.g. in the spirit outlined by Schmutz (1991). Progress with respect to this task is under way in our group.

Finally, one of our ultimate goals is the NLTE abundance determination of iron group elements from optical lines in extremely luminous A-type supergiants, related to our objective of calibrating and using the wind-momentum luminosity relation in distant galaxies (cf. Sect. 1). Due to the enormous number of lines to be considered, the exact calculation of all transitions might turn out as prohibitive if a fast solution is aimed at, although Hillier (1996) has made significant progress into this direction. For our purposes, we have to develop reliable criteria which will allow for a separation of lines into those to be treated in the CMF and those which can be approximated by the Sobolev transfer, without affecting the overall accuracy. This work has also been started.

Acknowledgements. We thank Dr. A.W. Fullerton, Prof. Dr. R.-P. Kudritzki and Dr. W. Schmutz for carefully reading the manuscript and useful comments. We also thank Dr. K. Butler for providing us with a number of plane-parallel, hydrostatic NLTE models and corresponding line profiles. This work has been partly funded by the Acciones Integradas hispano-alemanas, a joint program of the Spanish Ministerio de Educacion y Ciencia (MEC) and the German Deutscher Akademischer Austausch Dienst (DAAD). J.P. gratefully acknowledges a travel grant within the DFG-project Pa 477/1-2.

A. Atomic Data

In this section, we describe our atomic models for hydrogen and helium and the data used for calculating the Stark-broadening in the formal integrals.

Our hydrogen model consists of 10 NLTE levels, defined by their principal quantum number. Since we are not including magnetic fields in our calculations, no splitting of the l values is required.

Radiative ionization cross-sections are calculated using the hydrogenic expression, which is proportional to ν^{-3} . The appropriate Gaunt factors are taken from Gingerich (1964). For the collisional ionizations, a generic form is adopted (Mihalas 1978, p. 133), where the factor Γ is fitted in powers of temperature T (all levels but $n = 2$) or $\log T$ ($n = 2$ level). Free-free opacity is calculated using a hydrogenic form (Mihalas 1978) with Gaunt factors from Karzas & Latter (1961).

Our implementation of the treatment of lines requires only the oscillator strength as input for radiative processes; they are taken from Wiese et al. (1966). For collisional processes, we use the formula of Burke et al. (1967), scaled to the Sampson & Golden (1971) results.

The ionized helium model includes 14 levels, all of which are treated in full NLTE (with only one quantum number, n , to describe each level, and all possible transitions among them). Radiative bound-free and free-free cross-sections are calculated using the same formulae as for hydrogen, with the obvious changes. Collisional bound-free probabilities use the same two expressions as for hydrogen, where the four highest levels are treated in the manner described by Seaton (1962).

The oscillator strengths for radiative bound-bound transitions are also taken from Wiese et al. (1966). Collisional bound-bound cross-sections are those proposed by Hinnov (1966),

scaled to fit the results from Sampson and Golden (1971), as in the hydrogen case.

The much more complicated model of neutral helium consists of 27 levels, 14 for the singlet and 13 for the triplet configuration, all of which are treated in NLTE. For $n \leq 4$, all possible L values are considered, while for $5 \leq n \leq 8$ we take two *compressed* levels per n , one for the singlets and the other for triplets, packing the different L states into one.

The number of possible transitions and formulae used is also increased compared to hydrogenic ions. Dielectronic recombination is not included at present; however, this should be an only minor contribution since such a process becomes *dominant* for HeI only at around 10^6 K (Burgess 1964). In any case, high temperatures are reached only in the deepest layers of our models, where the electron density is large enough to produce collisional ionization before the stabilizing transition can take place (Burgess and Summers 1969).

Allowed (radiative and collisional) and forbidden (only collisional) HeI transitions are considered and treated, up to a total number of around 250. For the different formulae employed, we refer the reader to the paper by Butler & Giddings (1985), where they describe the major features of DETAIL and all the cross-sections implemented in it.

We now turn to the data used for calculating the Stark-broadening of hydrogen and helium. For neutral hydrogen, Vidal, Cooper & Smith (1970, 1971, 1973) have developed an *unified theory* which has proven to be highly accurate³. Schönig & Butler (1989a, 1989b) have extended this theory to HeII lines. Both groups have published tables of the corresponding line profiles under conditions of astrophysical interest. When the line we are considering is in the tables, we use their data; otherwise, we apply the theory of Griem (1960) as used by Auer & Mihalas (1972) with the improvements due to Simon (1979) to obtain Stark profiles for HeII lines. For neutral helium, we use tables computed with the theory of Barnard et al. (1969) for the lines at 4026 and 4388 Å, and that of Barnard et al. (1974) for those at 4922 and 4471 Å. For other HeI lines and in those cases where the tables for the upper four lines do not extend far enough in electron density, we use the “isolated line” approach described by Griem (1974).

B. The temperature stratification: NLTE Hopf function

The most tedious (and time-consuming) work in the construction of stellar atmospheres is the establishment of the temperature stratification from a rigorous treatment of radiative equilibrium. Considering the rather large number of present uncertainties, which at present influence the resulting structures (cf. Sect. 3.1), one may debate the extent to which this procedure is useful if we consider the expanding atmospheres of massive stars. Since it is of great importance, however, that the resulting atmospheres and line profiles are at least internally consistent –

³ In former theories, a different treatment was done for the line center, the transition zone, and the wings of the profile; *unified*, in this case, refers to a single treatment for the whole profile.

e.g., our results should reproduce the plane-parallel ones in cases of negligible winds – we have developed an approximate treatment of the problem which yields both the required consistency and costs almost no time and effort. This procedure consists of two steps, namely to adapt the results of available plane-parallel NLTE models (this section) and to relate them to the present situation of (spherically) atmospheres with a different density stratification (Appendix C).

The first step is based on a suggestion by R.-P. Kudritzki and exploits the fact that the decisive control parameter of the temperature run is the Rosseland opacity (and not, e.g., the column density). Thus, and at first neglecting the influence of sphericity, two models with different density structures should yield an analogous degree of flux conservation when both apply the same functional dependence $T(\tau_R)$. From this philosophy, it is straightforward to develop an adequate procedure. We take the output from a converged plane-parallel NLTE model available to our group –preferentially with the same elements as considered in the model to be constructed – and relate their apparent $T(\tau_R)$ stratification via the well-known formula for the grey case, i.e., we introduce a “NLTE Hopf function” $q_N(\tau_R)$ (Eq. 7). In this way, we account for NLTE effects leading to deviations from the grey case. Strictly speaking, this approach will only then result in the same degree of flux conservation if the τ_R -scale of the model to be constructed is also calculated on the basis of NLTE-opacities. However, due to the nature of Rosseland opacities which give the highest weight to the smallest opacities (which are then close to the pure Thomson background), the differences between $\tau_R(\text{LTE})$ and $\tau_R(\text{NLTE})$ are only small. Thus, significant differences of both scales, which would require an additional iteration cycle (not presently implemented in our code), are only to be expected if the ionization equilibrium of the dominant ions is drastically shifted due to NLTE effects.

Finally, and in order to obtain a practicable tool for establishing the new temperature structure, the NLTE Hopf function derived from the model output is parameterized in a way consistent with the (two-point) functional behaviour of the *grey* Hopf function (e.g., Mihalas 1978, p. 69), namely

$$q_N(\tau_R) \approx q_\infty + (q_0 - q_\infty) \exp(-\gamma \tau_R), \quad (\text{B1})$$

where q_0 , q_∞ and γ are fit parameters to the run of $q_N(\tau_R)$. These parameters are chosen in such a way that the fitted q_N stratification in the decisive part of the τ_R -scale – from $\tau_R \approx 3$ outwards to the temperature minimum (in the typical NLTE case at $\tau_R \approx 0.01$) – is the best compromise with the actual run. This approach implicitly assumes that $T(\tau_R) \approx T(q_0) = T_{\min}$ for $\tau_R < \tau_0$, if the temperature minimum is located at τ_0 (cf. the discussion in Sect. 3.1). Fig. 25 and 26 give some examples of the precision obtained, and Table 2 presents the parameters of the NLTE Hopf function for a number of models discussed in this paper.

Table 2. NLTE Hopf function parameterized as in Eq. B1 for a number of plane-parallel NLTE H/He models, all with $Y = N_{\text{He}}/N_{\text{H}} = 0.1$.

T_{eff}	$\log g$	q_∞	q_0	γ
50000	4.0	0.48	0.38	1.30
40000	4.0	0.82	0.48	1.63
37500	4.0	0.82	0.44	2.78
27500	3.0	1.05	0.33	0.73
	2.75	1.05	0.33	0.55
25000	3.0	1.00	0.30	0.80
	2.75	1.00	0.30	0.60
22500	3.0	0.85	0.28	0.70
	2.75	0.85	0.28	0.65
9500	1.5	0.70	0.42	3.00
	1.25	0.67	0.41	3.00
	0.9	0.52	0.37	3.00
8500	1.25	0.85	0.44	3.00
	1.0	0.80	0.44	3.00

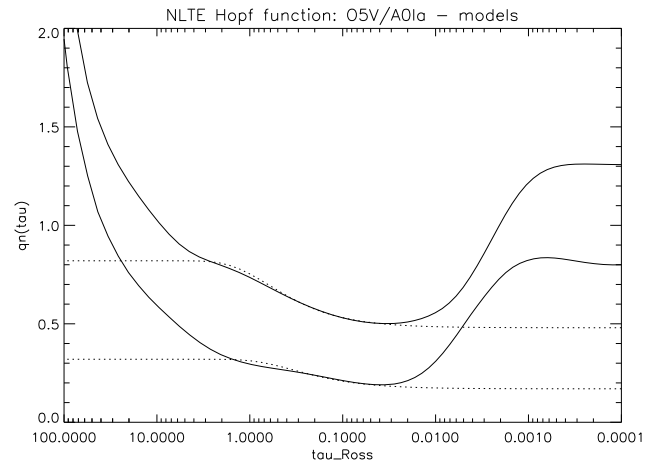


Fig. 25. NLTE Hopf function from plane-parallel NLTE H/He models OP2 (upper curves) and AP7 (lower curves, for parameters see Tab. 1). Dotted: approximation of Eq. B1 with parameters from Tab. A1. For convenience, both lower curves are shifted by -0.2 .

C. The temperature stratification: Inclusion of sphericity effects

The solution of the spherical grey problem has been extensively discussed by Hummer & Rybicki (1971 and references therein). However, instead of using their final (numerical) results, we require an approximate procedure which will allow us to generalize the approach of Appendix B for spherical geometries. In particular, we seek the appropriate transformation of the NLTE Hopf function derived from plane-parallel models to retain the flux-conserving properties (under NLTE conditions) of the scheme.

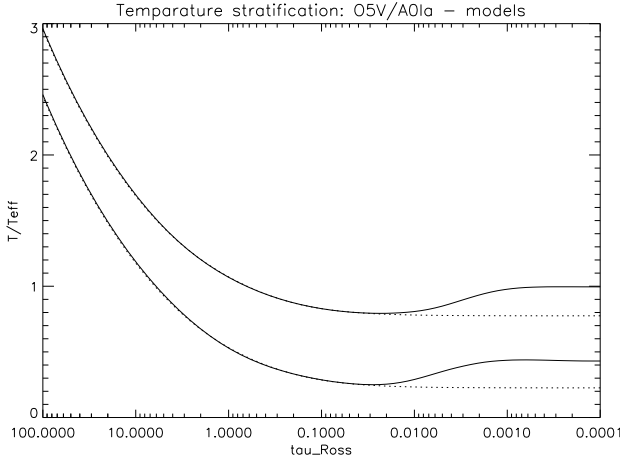


Fig. 26. Temperature stratification of plane-parallel NLTE H/He models OP2 (upper curves) and AP7 (lower curves). Dotted: Temperature structure from approximate NLTE Hopf function as in Fig. 25. For convenience, both lower curves are shifted by -0.5 .

In spherical atmospheres, the asymptotic behaviour of the grey mean intensity is well known:

$$\begin{aligned} J &\sim H_o \left(\frac{R_*}{r}\right)^2 (1 + \tau_R) & (\tau_R \rightarrow 0) \\ J &\sim 3 H_o \tau'_R + C & (\tau_R \rightarrow \infty). \end{aligned} \quad (\text{C1})$$

H_o is the photospheric Eddington flux, τ'_R is defined in Eq. 9 and C is an integration constant depending on the chosen boundary condition. Assuming now a power law stratification for the Rosseland opacity $\chi_R \sim r^{-n}$, the ratio of τ'_R and τ_R is simply given by

$$\frac{\tau'_R}{\tau_R} = \frac{n-1}{n+1} \left(\frac{R_*}{r}\right)^2. \quad (\text{C2})$$

In the outer atmospheres of the OBA-stars under consideration, Thomson-scattering dominates, so that with $n \approx 2$ we can write

$$\tau_R \approx 3\tau'_R \left(\frac{R_*}{r}\right)^2 \quad (\tau_R \rightarrow 0) \quad (\text{C3})$$

and thus, from Eq. C1

$$J \sim H_o \left(\frac{R_*^2}{r^2} + 3\tau'_R\right) \quad (\tau_R \rightarrow 0). \quad (\text{C4})$$

In the interior part of the atmosphere, we choose the integration constant in such a way that we can unify both regimes

$$J \sim H_o 3\tau'_R + C \rightarrow H_o \left(\left(\frac{R_*}{r}\right)^2 + 3\tau'_R\right) \quad (\tau'_R \rightarrow \infty), \quad (\text{C5})$$

and obtain (up to now from the LTE condition $J = B$)

$$T^4(r) = T_{\text{eff}}^4 \frac{3}{4} \left(\frac{R_*^2}{3r^2} + \tau'_R\right). \quad (\text{C6})$$

For power law opacities, this equation is equivalent to

$$T^4(r) = T_{\text{eff}}^4 \frac{3}{4} \frac{\tau'_R}{\tau_R} \left(\frac{n+1}{3(n-1)} + \tau_R\right). \quad (\text{C7})$$

Note that Eq. C7 agrees with the ‘‘conventional’’ spherical grey temperature law (Larson 1969), but has been derived here in a somewhat different spirit. This expression is now (almost) consistent with the analogous plane-parallel one. In this limit, $\tau'_R = \tau_R$ and the offset in τ_R -scale relates well to the corresponding one in the Eddington-approximation, namely $(n+1)/(3(n-1)) = 1/2$ for $n = 2$ and $= 5/9$ for $n = 4$, compared to the plane-parallel value of $2/3$. Thus, we demand that the NLTE Hopf function derived from plane-parallel models (see above) shall correspond to this quantity and finally have

$$T^4(r) = T_{\text{eff}}^4 \frac{3}{4} \frac{\tau'_R}{\tau_R} (q_N(\tau_R) + \tau_R) = T_{\text{eff}}^4 \frac{3}{4} (q'_N(\tau'_R) + \tau'_R) \quad (\text{C8})$$

where the spherical analog of the NLTE Hopf function has been defined by

$$q'_N(\tau'_R) := \frac{\tau'_R}{\tau_R} q_N(\tau_R). \quad (\text{C9})$$

D. Calculation of net continuum rates in the ALI formalism

In this appendix, we describe how we include the ionization/recombination integrals into the rate equations. As pointed out in Sect. 2.3, it is especially this formulation where our approach differs mostly from other codes, except perhaps ISA (de Koter et al. 1993), which applies a similar philosophy. Since in our opinion the formulation of the net continuum rates is the very heart of any NLTE code and decisively controls the stability and convergence speed, we will give here our solution to the problem in some detail.

To begin with, the net continuum rate between transition $k \rightarrow l$ is defined as

$$\mathbf{A} = n_k R_{kl} - n_l R_{lk} \quad (\text{D1})$$

with lower occupation number n_l , upper occupation number n_k (in the continuum with respect to n_l), recombination rate $n_k R_{kl}$ and ionization rate $n_l R_{lk}$. With ionization and recombination rates written explicitly, we obtain

$$\begin{aligned} \mathbf{A} &= 4\pi n_k \left(\frac{n_l}{n_k}\right)^* \int \frac{\alpha_{lk}(\nu)}{h\nu} \left(\frac{2h\nu^3}{c^2} + J_\nu\right) e^{-h\nu/kT} d\nu \\ &\quad - 4\pi n_l \int \frac{\alpha_{lk}(\nu)}{h\nu} J_\nu d\nu. \end{aligned} \quad (\text{D2})$$

The integration is understood to be performed always between threshold frequency and – formally – infinity. Rearranging with respect to the mean continuum intensity J_ν , we have

$$\mathbf{A} = 4\pi n_k \left(\frac{n_l}{n_k}\right)^* \int \frac{\alpha_{lk}(\nu) 2h\nu^3}{h\nu c^2} e^{-h\nu/kT} d\nu + 4\pi \int \frac{\alpha_{lk}(\nu)}{h\nu} \left[n_k \left(\frac{n_l}{n_k}\right)^* e^{-h\nu/kT} - n_l \right] J_\nu d\nu, \quad (\text{D3})$$

where an asterisk denotes the usual LTE ratio (given by the Saha-Boltzmann factor). Before we can further proceed, we have to establish the relation between mean intensity and source function with regard to the ALI-formalism.

The complete continuum source function can be written as:

$$S_\nu = \frac{\eta_\nu}{\chi_\nu} = \frac{\eta^\dagger + \sigma_e J_\nu}{\chi^\dagger + \sigma_e} =: S_\nu^q + TH_\nu \cdot J_\nu \quad (\text{D4})$$

where the superscript “†” denotes the *thermal* part of emissivity and opacity, σ_e is the Thomson opacity and S^q the “quasi-thermal” (because of the Thomson contribution to the opacity) source function. Note that we have omitted the frequential dependence of η^\dagger and χ^\dagger to avoid an accumulation of indices.

These thermal quantities include the contribution from all transitions involved, so that with

$$\begin{aligned} \eta^\dagger &= \sum_i \eta_i^\dagger; & \chi^\dagger &= \sum_i \chi_i^\dagger \\ \beta_i &= \frac{\chi_i^\dagger}{\chi^\dagger + \sigma_e} \\ S_i^q &= \frac{\eta_i^\dagger}{\chi_i^\dagger} = \frac{2h\nu^3}{c^2} \frac{1}{\frac{n_l}{n_k} \left(\frac{n_k}{n_l}\right)^* e^{h\nu/kT} - 1} \end{aligned} \quad (\text{D5})$$

the quasi-thermal source function can be expressed as

$$S^q = \frac{\sum_i \eta_i^\dagger}{\chi^\dagger + \sigma_e} = \sum_i \frac{\eta_i^\dagger}{\chi_i^\dagger} \frac{\chi_i^\dagger}{\chi^\dagger + \sigma_e} = \sum_i \beta_i S_i^q, \quad (\text{D6})$$

and with Eq. (D4) the ALI formalism reads (e.g., Werner & Husfeld 1985)

$$\begin{aligned} J^{(n)} &= \Lambda^* S^{q(n)} + \Lambda^* TH^{(n)} \cdot J^{(n)} \\ &+ \Lambda S^{(n-1)} - \Lambda^* S^{q(n-1)} - \Lambda^* TH^{(n-1)} \cdot J^{(n-1)}. \end{aligned} \quad (\text{D7})$$

The indices n and $(n-1)$ account for the iteration step in which the corresponding quantities have been calculated, Λ is the usual Lambda-Operator acting on S_ν and Λ^* the appropriate ALO. By assuming the Thomson coefficient, TH , to remain constant between two consecutive iterations, this equation can be put in a more compact form,

$$J^{(n)} = \frac{\Lambda^* (S^{q(n)} - S^{q(n-1)})}{1 - \Lambda^* TH} + J^{(n-1)}. \quad (\text{D8})$$

The result of this different formulation is a considerable acceleration of the convergence rate in cases of an optically thick scattering continuum (e.g., for frequencies far away from

the edges), since the amplification “matrix” (Olson et al. 1986) obtains large values as $\Lambda^* TH \rightarrow 1$.

Introducing this equation for J in Eq. (D3), we can in principle calculate the corresponding terms in the rate equations. The problem that arises now is the well known non-linearity related with this procedure: the current source function, $S^{q(n)}$, depends on the actual populations, which are still unknown; when the dependence is explicitly written, the resulting expression to be inserted in \mathbf{A} is non-linear. To avoid the problem of solving a set of N (number of levels) coupled non-linear equations, it is customary to manipulate the equations in order to retain linearity, typically by using some non-linear terms from the *previous* iteration. That is what Rybicki (1971) called *preconditioning*, and some authors (e.g., Herrero 1987, Voels et al. 1989, Rybicki & Hummer 1991) apply this idea in their codes. Preconditioning, in principle, decreases the power of the ALI cycle, as not *all* the information from the current source function, $S^{(n)}$, is used, but the gain in computational time is large enough to prefer it. Other methods to solve this problem are the *complete linearization*, developed by Auer & Mihalas (1969), which is restricted to a rather limited number of levels, and the formulation by Pauldrach & Herrero (1988), which uses the results from the two previous iterations. (As an alternative to ALI and complete linearization, we mention here also the newly rediscovered method of successive overrelaxation (SOR, cf. Trujillo Bueno & Fabiani Bendicho 1995)).

We will follow the philosophy of preconditioning, however in our own formulation. The non-linearity appears because of the term $S^{q(n)} - S^{q(n-1)}$ in Eq. (D8), which is removed by an approximate treatment of Eq. (D6): for each transition $l \rightarrow k$, we suppose

$$S^q = \sum_i \beta_i S_i^q \simeq \beta_{lk} S_{lk}^q, \quad (\text{D9})$$

which is equivalent to assuming that the transition under consideration is the dominant one, but weighting it by its real contribution to the total (quasi-thermal) source function.

Are we allowed to make such an approximation? Certainly, since $\beta_{lk} < 1$ by definition and thus $\Lambda^* \beta_{lk} < \Lambda^*$, i.e., our modified ALO still underestimates the real Λ operator, which ensures convergence (cf. Puls & Herrero 1988).

The second assumption of our approach is to require the ratio (which is much better than any absolute value) β_{lk} between transition opacity and total opacity to remain constant between iteration $(n-1)$ and n , so that Eq. (D8) finally obtains the form

$$J^{(n)} = \frac{\Lambda^* \beta_{lk}^{(n-1)} (S_{lk}^{q(n)} - S_{lk}^{q(n-1)})}{1 - \Lambda^* TH} + J^{(n-1)}. \quad (\text{D10})$$

Thus, we can remove the non-linear part in the second term of equation (D3) via the definition of the thermal source function and achieve linearity in both n_l and n_k :

$$\left[n_k \left(\frac{n_l}{n_k}\right)^* e^{-h\nu/kT} - n_l \right] J^{(n)} =$$

$$= \left[n_k \left(\frac{n_l}{n_k} \right)^* e^{-h\nu/kT} - n_l \right] \left[J^{(n-1)} - \frac{\Lambda^* \beta_{lk}^{(n-1)} S_{lk}^{t(n-1)}}{1 - \Lambda^* TH} \right] - n_k \left(\frac{n_l}{n_k} \right)^* \frac{2h\nu^3}{c^2} e^{-h\nu/kT} \frac{\Lambda^* \beta_{lk}^{(n-1)}}{1 - \Lambda^* TH} \quad (\text{D11})$$

In order to find a compact expression for \mathbf{A} , we use the definition of χ_{lk}^t for calculating β_{lk} ,

$$\chi_{lk}^t = \alpha_{lk}(\nu) \left[n_l - n_k \left(\frac{n_l}{n_k} \right)^* e^{-h\nu/kT} \right] \quad (\text{D12})$$

and finally obtain the net continuum rate

$$\mathbf{A} = 4\pi n_k \left(\frac{n_l}{n_k} \right)^* (I_1 - I_2) - 4\pi n_l (I_3 - I_4) \quad (\text{D13})$$

with integrals I_1 to I_4

$$I_1 = \int \frac{\alpha_{lk}(\nu)}{h\nu} e^{-h\nu/kT} \left[\frac{2h\nu^3}{c^2} + J_\nu^{(n-1)} \right] d\nu$$

$$I_2 = \int \frac{\alpha_{lk}(\nu)}{h\nu} \frac{2h\nu^3}{c^2} e^{-h\nu/kT} \frac{\Lambda^* \alpha_{lk}(\nu)}{(1 - \Lambda^* TH)} \frac{n_l^{(n-1)}}{(\chi^t + \sigma_e)} d\nu$$

$$I_3 = \int \frac{\alpha_{lk}(\nu)}{h\nu} J_\nu^{(n-1)} d\nu$$

$$I_4 = \int \frac{\alpha_{lk}(\nu)}{h\nu} \frac{2h\nu^3}{c^2} e^{-h\nu/kT} \frac{\Lambda^* \alpha_{lk}(\nu)}{(1 - \Lambda^* TH)} \frac{n_k^{(n-1)} \left(\frac{n_l}{n_k} \right)^*}{(\chi^t + \sigma_e)} d\nu.$$

In passing, we note that Eq. D13 results in the usual Lambda iteration for $\Lambda^* = 0$, whereas for $\beta_{lk} = 1$ (only one transition present) and $TH = 0$ (no electron scattering) this equation is consistent with the usual ALI formulation for local ALOs.

E. Separation of line and continuum transfer in the formal integral

In the following section, we develop a formalism to separate the line and continuum transfer in the formal integral. This approach can save a large amount of computational time in those cases, where

- i. the integral is solved on a radial micro-grid (cf. Sect. 2.4.1).
- ii. the resonance zones have an only small spatial extent compared to the rest of the ray.
- iii. the continuum source function is approximately frequency-independent over the line profile under consideration.

The maximum gain in computational speed by using the following approach is thus obtained if we consider pure Doppler profiles and a “simple” continuum source function. However, even for Stark-broadening a substantial acceleration is achieved, since this effect is present only in the lower atmosphere. In order to apply this approach universally, we have included the case of a frequency dependent source function, e.g., non-coherent e^- -scattering. If this option is chosen (which is necessary only for winds with a large \dot{M} or a significant photon injection rate

from below the electron-scattering sphere), then the temporal advantage of the procedure is lost.

Under the assumption that the frequential variation of the continuum opacity over the line profile can be neglected, the transfer equation along a certain ray (usual $p - z$ -geometry provided) can be written as

$$\frac{dI(z, x)}{dz} = \chi_l(z, x_0) (S_l(z) - I(z, x)) + \chi_c(z) (S_c(z, x_0) - I(z, x)), \quad (\text{E1})$$

where x and x_0 are the observer’s and CMF-frequency in units of the wind’s maximum Doppler shift

$$x = \frac{\nu - \nu_l}{\nu_l} \frac{c}{v_\infty}$$

$$x_0 = \frac{\nu_{\text{CMF}} - \nu_l}{\nu_l} \frac{c}{v_\infty} = x - \mu \frac{v(z)}{v_\infty} \quad (\text{E2})$$

(ν_l is the transition frequency). We now define a transformed intensity via

$$\tilde{I}(z, x) = I(z, x) U_c(z) - \int_{z_{\min}}^z U_c(z') S_c(z', x_0) \chi_c(z') dz', \quad (\text{E3})$$

with

$$U_c(z) = \exp \left[\int_{z_{\min}}^z \chi_c(z') dz' \right]. \quad (\text{E4})$$

Defining also a transformed source function, \tilde{S}_1 ,

$$\tilde{S}_1(z, x) = U_c(z) S_l(z) - \int_{z_{\min}}^z U_c(z') S_c(z', x_0) \chi_c(z') dz', \quad (\text{E5})$$

it is straightforward to derive a *transformed equation of transfer*

$$\frac{d\tilde{I}(z, x)}{dz} = \chi_l(z, x_0) (\tilde{S}_1(z, x) - \tilde{I}(z, x)). \quad (\text{E6})$$

The reader should note that this equation corresponds to the transfer equation for the pure line case, i.e., it has to be solved only inside the resonance zone(s). (One zone per ray and line component, unless the components overlap within their intrinsic profiles). In between, the transformed intensity remains constant. Up to this point, we have strictly followed the procedure introduced by Hummer & Rybicki (1985) in order to derive a “Sobolev approximation with continuum”. From now on, our approach is different, since we consider the “exact” case. With the obvious boundary conditions

$$U_c(z_{\min}) = 1$$

$$\tilde{I}(z_{\min}, x) = I(z_{\min}, x) \quad (\text{E7})$$

the transformed transfer equation has the well-known solution

$$\tilde{I}(z_{\max}, x) = I(z_{\min}, x)e^{-\tau_1(z_{\min}, x)} + \int_{z_{\min}}^{z_{\max}} \tilde{S}_1(z', x)e^{-\tau_1(z', x)}\chi_1(z', x_0)dz' \quad (\text{E8})$$

with an optical depth τ_1

$$\tau_1(z, x) = \int_z^{z_{\max}} \chi_1(z', x_0)dz'. \quad (\text{E9})$$

In principle, we can calculate \tilde{I} at every position along the ray, but in the following we are only interested in its value at z_{\max} to obtain emergent intensities and fluxes. Transforming back by means of Eq. (E3), the emergent intensity reads

$$I(z_{\max}, x) = \frac{1}{U_c(z_{\max})} \times \left[\tilde{I}(z_{\max}, x) + \int_{z_{\min}}^{z_{\max}} U_c(z')S_c(z', x_0)\chi_c(z')dz' \right]. \quad (\text{E10})$$

Using the continuum optical depth along the ray,

$$\tau_c(z) = \int_z^{z_{\max}} \chi_c(z')dz', \quad (\text{E11})$$

we can write $I(z_{\max})$ in a more compact way,

$$I(z_{\max}, x) = \tilde{I}(z_{\max}, x)e^{-\tau_c^{\max}} + F_s(0, x), \quad (\text{E12})$$

where

$$\tau_c^{\max} = \tau_c(z_{\min})$$

$$F_s(\tau_c, x) = \int_{\tau_c}^{\tau_c^{\max}} S_c(\tau_c', x_0)e^{-\tau_c'}d\tau_c'.$$

Note that τ_c and F_s consist of pure continuum quantities and have to be calculated only once per line profile (unless S_c becomes frequency dependent, see above). With these notations, the transformed line source function becomes

$$\tilde{S}_1(z, x) = e^{\tau_c^{\max}} \left(S_1(z)e^{-\tau_c(z)} - F_s[\tau_c(z), x] \right), \quad (\text{E13})$$

so that the integral for the emergent intensity is finally given by

$$I(z_{\max}, x) = I(z_{\min}, x)e^{-(\tau_1^{\max} + \tau_c^{\max})} + F_s(0, x) + \int_{z_{\min}}^{z_{\max}} \left(S_1(z')e^{-\tau_c(z')} - F_s[\tau_c(z'), x] \right) e^{-\tau_1(z', x)}\chi_1(z', x_0)dz'. \quad (\text{E14})$$

The advantages of this formula compared to the conventional solution are obvious. After having established our micro-grid (typically with five points per thermal Doppler velocity, see Sect. 2.4.1) we can calculate all continuum quantities ($\tau_c(z)$ and $F_s(\tau_c(z))$) in advance and find, per ray and frequency, the boundaries of the resonance zone(s). This can be done without much computational effort, if we organize the profile calculation in

such a way that the *outer loop comprises the angular integration (p-rays) and the inner loop is the frequential one*. In this case then and when we proceed from one observer's frequency to the next, the boundaries of the resonance zones are shifted by only a few number of depth points which can be found almost instantaneously due to our micro-grid concept.

Inside the resonance zones, we calculate the modified line source function (bracketed term above) and calculate the integral. Outside the resonance zones, nothing has to be done. Having integrated throughout a given ray, the emergent intensity is obtained by adding the first two terms in Eq. E14.

Hence, in the most favourable case of pure Doppler profiles, we have to perform typically 30 integration steps per ray, frequency and component. (assuming a width of ± 5 thermal Doppler widths).

References

- Abbott D.C., Hummer D.G., 1985, ApJ 288, 679
Auer L., 1976, JQSRT 16, 931
Auer L.H., Mihalas D., 1969, ApJ 158, 641
Auer L.H., Mihalas D., 1972, ApJS 24, 193
Auer L.H., Van Blerkom D., 1972, ApJ 178, 175
Barlow M.J., Cohen L., 1977, ApJ 213, 737
Barnard A.J., Cooper J., Shamey L.J., 1969, A&A 1, 28
Barnard A.J., Cooper J., Smith E.W., 1974, JQSRT 14, 1025
Bjorkman J.E., Cassinelli J.P., 1993, ApJ 409, 429
Burgess A., 1964, ApJ 139, 776
Burgess A., Summers H., 1969, ApJ 157, 1007
Burke P.G., Ormonde S., Whitaker W., 1967, Proc. Phys. Soc. 92, 319
Butler K., Giddings J.R., 1985, Coll. Comp. Project No. 7 (CCP7), Newsletter 9, London, p. 7
Crowther P.A., Smith L.J., Hillier D.J., 1995a, A&A 293, 403
Crowther P.A., Smith L.J., Hillier D.J., 1995b, A&A 302, 457
de Koter A., Schmutz W., Lamers H.J.G.L.M., 1993, A&A 277, 561
de Koter A., Lamers H.J.G.L.M., Schmutz W., 1996, A&A 306, 501
Dreizler S., Werner K., 1992, in: The Atmospheres of Early Type Stars, eds U. Heber & C.S. Jefferey. Kluwer, Lecture Notes in Physics 401, p. 436
Drew J.E., 1989, ApJS 71, 267
Feldmeier A., 1995, A&A 299, 523
Feldmeier A., Kudritzki R.-P., Palsa R., Pauldrach A.W.A., Puls J., 1996, A&A, in press
Gabler R., 1991, Thesis, Ludwig-Maximilians-Universität München
Gabler R., Gabler A., Kudritzki R.P., Puls J., Pauldrach A.W.A., 1989, A&A 226, 162
Gingerich O., 1964, in: First Harvard-Smithsonian Conference on Stellar Atmospheres, p. 17
Griem H.R., 1960, ApJ 132, 883
Griem H.R., 1974, Spectral Line Broadening by Plasmas. Academic Press, New York
Gruschinske J., Kudritzki R.P., 1979, A&A 77, 341
Hamann W.R., 1981, A&A 93, 353
Hamann W.R., Schmutz W., 1987, A&A 174, 173
Hamann W.R., Dünnebeil G., Koesterke L., Wessolowski U., Schmutz W., 1991, A&A 249, 443
Herrero A., 1987, A&A 171, 189
Herrero A., 1994, in: Evolution of Massive Stars, eds. D. Vanbeveren, W. van Rensbergen & C. de Loore. Kluwer, Dordrecht, p. 137

- Herrero A., Kudritzki R.P., Vilchez J.M., Kunze D., Butler K., Haser S., 1992, *A&A* 261, 209
- Herrero A., Kudritzki R.P., Gabler R., Vilchez J.M., Gabler A., 1995, *A&A* 297, 556
- Hillier D.J., 1984, *ApJ* 280, 744
- Hillier D.J., 1989, *ApJ* 347, 392
- Hillier D.J., 1991, *A&A* 247, 455
- Hillier D.J., 1996, in: *WR Stars in the Framework of Stellar Evolution*, 33rd Liege Int. Astroph. Coll., in press
- Hillier D.J., Kudritzki R.-P., Pauldrach A.W.A., Baade D., Cassinelli J.P., Puls J., Schmitt J.H.M.M., 1993, *A&A* 276, 117
- Hinnov E., 1966, *J. Opt. Soc. Am.* 56, 1179
- Hubený I., Leitherer J., 1989, in: *IAU Coll. 113, Physics of Luminous Blue Variables*, eds. K. Davidson, A.F.J. Moffat & H.J.G.L.M. Lamers. Kluwer, Dordrecht, p. 283
- Hummer D.G., Rybicki G.B., 1971, *MNRAS* 152, 1
- Hummer D.G., Rybicki G.B., 1985, *ApJ* 293, 258
- Kaufert A., Stahl O., Wolf B., Gäng T., Gummertsbach C.A., Kóvacs J., Mandel H., Szeifert T., 1996, *A&A* 305, 887
- Karzas W.J., Latter R., 1961, *ApJS* 6, 167
- Klein R.I., Castor J.I., 1978, *ApJ* 220, 902
- Kudritzki R.-P., 1976, *A&A* 52, 11
- Kudritzki R.P., Lennon D.J., Puls J., 1995, in: *Science with the Very Large Telescope*, eds. J.R. Walsh & I.J. Danziger. ESO Astrophysics Symposia, Springer, Heidelberg, p. 246
- Lamers H.J.G.L.M., Cerruti-Sola M., Perinotto M., 1987, *ApJ* 314, 726
- Lamers H.J.G.L.M., Leitherer C., 1993, *ApJ* 412, 771
- Langer N., Maeder A., 1995, *A&A* 295, 685
- Larson R.B., 1969, *MNRAS* 145, 297
- Lanz T., de Koter A., Hubeny I., Heap S.R., 1996, *ApJ* 465, 359
- MacFarlane J.J., Waldron W.L., Corcoran M.F., Wolff M.J., Wang P., Cassinelli J.P., 1993, *ApJ* 419, 813
- MacFarlane J.J., Cohen D.H., Wang P., 1994, *ApJ* 437, 351
- Massa D., et al., 1995, *ApJ* 452, L53
- McCarthy J.K., Lennon D.J., Venn K.A., Kudritzki R.-P., Puls J., Najjarro F., 1995, *ApJ* 455, L135
- Mihalas D., 1978, *Stellar Atmospheres*, 2nd Edition. Freeman, San Francisco
- Mihalas D., Hummer D.G., 1974, *ApJS* 265, 343
- Mihalas D., Kunasz P., Hummer D.G., 1975, *ApJ* 202, 465
- Mihalas D., Kunasz P., Hummer D.G., 1976, *ApJ* 210, 419
- Olson G.L., Auer L., Buchler J.R., 1986, *JQSRT* 35, 431
- Owocki S.P., Castor J.I., Rybicki G.G., 1988, *ApJ* 335, 914
- Owocki S.P., Cranmer S.R., Fullerton A.W., 1995, *ApJ* 453, L37
- Pauldrach A.W.A., Herrero A., 1988, *A&A* 199, 262
- Pauldrach A.W.A., Puls J., 1990, *A&A* 237, 409
- Pauldrach A.W.A., Puls J., Kudritzki R.P., 1986, *A&A* 164, 86
- Pauldrach A.W.A., Kudritzki R.P., Puls J., Butler K., Hunsinger J., 1994, *A&A* 283, 525
- Petrenz P., Puls J., 1996, *A&A*, in press
- Puls J., 1991, *A&A* 248, 581
- Puls J., Herrero A., 1988, *A&A* 204, 219
- Puls J., Hummer D.G., 1988, *A&A* 191, 87
- Puls J., Pauldrach A.W.A., 1990, in: *Properties of hot luminous stars*, Boulder-Munich workshop, ed. C.D. Garmany, PASPC 7, p. 203
- Puls J., Kudritzki R.-P., Herrero A., Pauldrach A.W.A., Haser S.M., Lennon D.J., Gabler R., Voels S.A., Vichez J.M., Wachter S., Feldmeier A., 1996, *A&A* 305, 171
- Prinja R.K., Massa D., Fullerton A.W., 1995, *ApJ* 452, L61
- Rybicki G.B., 1971, in: *Line Formation in Magnetic Fields*. National Center for Atmospheric Research, Boulder
- Rybicki G.B., Hummer D.G., 1978, *ApJ* 219, 654
- Rybicki G.B., Hummer D.G., 1991, *A&A* 245, 171
- Rybicki G.B., Hummer D.G., 1994, *A&A* 290, 553
- Sampson D.H., Golden L.B., 1971, *ApJ* 170, 169
- Santolaya-Rey A.E., 1995, Thesis, Instituto de Astrofísica de Canarias, La Laguna
- Schaerer D., Schmutz W., 1994, *A&A* 288, 231
- Schöning T., Butler K., 1989a, *A&AS* 78, 51
- Schöning T., Butler K., 1989b, *A&AS* 79, 153
- Schmutz W., 1991, in: *Stellar Atmospheres: Beyond Classical Models*, eds. L. Crivellari, I. Hubeny and D.G. Hummer, NATO ASI Series C Vol. 341, Kluwer, Dordrecht, p. 191
- Schmutz W., Hamann W.R., Wessolowski U., 1989, *A&A* 210, 236
- Seaton M.J., 1962, in: *Atomic and Molecular Processes*. Academic Press, New York
- Sellmaier F., 1996, Thesis, Ludwig-Maximilians-Universität München
- Sellmaier F., Puls J., Kudritzki R.P., Gabler A., Gabler R., Voels S., 1993, *A&A* 273, 533
- Simon K.P., 1979, Thesis, Christian-Albrechts-Universität zu Kiel
- Stahl O., Aab O., Smolinski J., Wolf B., 1991, *A&A* 252, 693
- Taresch G., 1991, Diploma Thesis, Ludwig-Maximilians-Universität München
- Taresch G., Kudritzki R.P., Hurwitz M., Bowyer S., Pauldrach A.W.A., Puls J., Bytler K., Lennon D.J., Haser S.M., 1996, *A&A*, submitted
- Trujillo Bueno J., Fabiani Bendicho P., 1995, *ApJ* 455, 646
- Vidal C.R., Cooper J., Smith E.W., 1970, *JQSRT* 10, 10011
- Vidal C.R., Cooper J., Smith E.W., 1971, *Nat. Bur. Stand. Monogr.* 120
- Vidal C.R., Cooper J., Smith E.W., 1973, *ApJS* 25, 37
- Voels S.A., Bohannan B., Abbott D.C., Hummer D.G., 1989, *ApJ* 340, 1073
- Waters, L.B.F.M., Wesselius, P.R., 1986, *A&A* 155, 104
- Werner K., 1992, in: *The Atmospheres of Early Type Stars*, eds U. Heber & C.S. Jefferey. Kluwer, Lecture Notes in Physics 401, p. 273
- Werner K., Husfeld D., 1985, *A&A* 148, 417
- Wiese W., Smith M., Glennon B., 1966, *Atomic Transition Probabilities*, Vol. 1: Hydrogen through Neon. U.S. Dept. of Commerce, Washington D.C.